# Angular Distribution Models for Top-of-Atmosphere Radiative Flux Estimation from the Clouds and the Earth's Radiant Energy System Instrument on the Tropical Rainfall Measuring Mission Satellite. Part II: Validation

NORMAN G. LOEB

*Center for Atmospheric Sciences, Hampton University, Hampton, Virginia*

KONSTANTIN LOUKACHINE

*Science Applications International Corporation, Hampton, Virginia*

NATIVIDAD MANALO-SMITH

*Analytical Services and Materials, Inc., Hampton, Virginia*

BRUCE A. WIELICKI AND DAVID F. YOUNG

*NASA Langley Research Center, Hampton, Virginia*

(Manuscript received 12 December 2002, in final form 7 June 2003)

ABSTRACT

Top-of-atmosphere (TOA) radiative fluxes from the Clouds and the Earth's Radiant Energy System (CERES) are estimated from empirical angular distribution models (ADMs) that convert instantaneous radiance measurements to TOA fluxes. This paper evaluates the accuracy of CERES TOA fluxes obtained from a new set of ADMs developed for the CERES instrument onboard the Tropical Rainfall Measuring Mission (TRMM). The uncertainty in regional monthly mean reflected shortwave (SW) and emitted longwave (LW) TOA fluxes is less than 0.5 W $m^{-2}$, based on comparisons with TOA fluxes evaluated by direct integration of the measured radiances. When stratified by viewing geometry, TOA fluxes from different angles are consistent to within 2% in the SW and 0.7% (or 2 W $m^{-2}$) in the LW. In contrast, TOA fluxes based on ADMs from the Earth Radiation Budget Experiment (ERBE) applied to the same CERES radiance measurements show a 10% relative increase with viewing zenith angle in the SW and a 3.5% (9 W $m^{-2}$) decrease with viewing zenith angle in the LW. Based on multiangle CERES radiance measurements, 1° regional instantaneous TOA flux errors from the new CERES ADMs are estimated to be $<$10 W $m^{-2}$ in the SW and $<$3.5 W $m^{-2}$ in the LW. The errors show little or no dependence on cloud phase, cloud optical depth, and cloud infrared emissivity. An analysis of cloud radiative forcing (CRF) sensitivity to differences between ERBE and CERES TRMM ADMs, scene identification, and directional models of albedo as a function of solar zenith angle shows that ADM and clear-sky scene identification differences can lead to an 8 W $m^{-2}$ root-mean-square (rms) difference in 1° daily mean SW CRF and a 4 W $m^{-2}$ rms difference in LW CRF. In contrast, monthly mean SW and LW CRF differences reach 3 W $m^{-2}$. CRF is found to be relatively insensitive to differences between the ERBE and CERES TRMM directional models.

## 1. Introduction

The Clouds and the Earth's Radiant Energy System (CERES) investigates the critical role that clouds and aerosols play in modulating the radiative energy flow within the earth–atmosphere system (Wielicki et al. 1995). The CERES effort builds upon the foundation of the Earth Radiation Budget Experiment (ERBE) (Barkstrom 1984) by providing accurate top-of-atmosphere (TOA) radiative fluxes together with coincident cloud and aerosol properties inferred from high-resolution imager measurements.

The CERES instrument measures radiances in three channels: a shortwave channel (0.3–5 $\mu$m) to measure reflected sunlight, a window channel to measure Earth-emitted thermal radiation in the 8–12-$\mu$m "window" region, and a total channel (0.3–200 $\mu$m). After removing the influence of instrument spectral response from the measurements (Loeb et al. 2001), CERES radiances are converted to reflected shortwave (SW), emitted longwave (LW), and emitted window (WN) TOA radiative fluxes. The radiance-to-flux conversion involves applying scene-dependent empirical angular dis-

*Corresponding author address:* Dr. Norman G. Loeb, Mail Stop 420, NASA Langley Research Center, Hampton, VA 23681-2199.
E-mail: n.g.loeb@larc.nasa.gov

tribution models (ADMs) constructed from several months of CERES data. In Part I of this study, Loeb et al. (2003) provided a detailed description of the methodology used to construct the CERES Tropical Rainfall Measuring Mission (TRMM) ADMs.

The objective of this paper is to estimate the accuracy of TOA fluxes generated from the new CERES TRMM ADMs through detailed comparisons between regional ADM-derived TOA fluxes and TOA fluxes evaluated by direct integration of the measured radiances, and through self-consistency tests to examine whether the ADM-derived TOA fluxes show any systematic dependence upon satellite viewing geometry. In order to compare the results with ERBE, the same set of consistency tests are also performed using TOA fluxes from the CERES ''ERBE-like'' product, which uses the ERBE scene identification and ADMs to derive TOA fluxes from CERES measurements. A separate analysis is also performed to examine the sensitivity in regional cloud radiative forcing to changes in ADMs, scene identification, and directional models of albedo as a function of solar zenith angle for two regions—one in the west Pacific Ocean, and the other in the east Pacific Ocean.

## 2. Observations

CERES TRMM was launched on 27 November 1997 in a 350-km circular precessing orbit with a 35° inclination angle. The TRMM satellite has a 46-day repeat cycle, so a full range of solar zenith angles over a region is acquired every 46 days. On TRMM, CERES has a spatial resolution of approximately 10 km (equivalent diameter) and operates in three scan modes: cross-track, alongtrack, and rotating azimuth plane (RAP) modes. In RAP mode the instrument scans in elevation as it rotates in azimuth, thus, acquiring radiance measurements from a wide range of viewing configurations. The CERES instrument on TRMM was shown to provide an unprecedented level of calibration stability ($\approx$0.25%) between in-orbit and ground calibration (Priestley et al. 1999). Unfortunately, the CERES TRMM instrument suffered a voltage converter anomaly and acquired only 9 months of scientific data.

All 9 months of the CERES TRMM single scanner footprint TOA/surface fluxes and clouds (SSF) product between 38°S and 38°N from January through August 1998 and March 2000 are considered. The CERES SSF product combines CERES radiances and fluxes with scene identification information inferred from coincident high spatial and spectral resolution Visible and Infrared Scanner (VIRS) measurements (Kummerow et al. 1998) and meteorological fields based on European Centre for Medium-Range Weather Forecasts (ECMWF) data assimilation analysis (Rabier et al. 1998). A comprehensive description of all parameters appearing in the CERES SSF product is provided in the CERES collection guide (Geier et al. 2003).

During the 9 months of CERES data acquisition, CERES was in a cross-track scan mode for 192 days, a RAP scan mode for 68 days, and an alongtrack scan mode for 9 days. Only CERES footprints that at least partially lie within the VIRS imager swath and whose centroids can be located on the earth's surface are retained in the SSF product. Because VIRS scans in the cross-track direction to a maximum viewing zenith angle of 49°, CERES footprints with viewing zenith angles $>49°$ do not appear in the SSF product when CERES is in a cross-track scan mode. Footprints with viewing zenith angles $>49°$ are available in the SSF product only when the CERES scans in either a RAP or alongtrack mode.

TOA fluxes in the SSF product are compared with TOA fluxes in the CERES ERBE-like product on a footprint-by-footprint basis. The CERES ERBE-like product is produced in order to extend the historical record of Earth radiation budget observations by processing CERES measurements with algorithms developed during ERBE (Smith et al. 1986). Therefore, ERBE-like TOA fluxes are determined using the ERBE ADMs (Suttles et al. 1988; Suttles et al. 1989) to convert CERES radiances to TOA fluxes, and the ERBE maximum likelihood estimation (MLE) technique is used to determine scene type (Wielicki and Green 1989). Note that because the ERBE-like product is produced independently of VIRS, all CERES field-of-views (FOVs) are retained in this product. However, in order to compare TOA fluxes from the ERBE-like and SSF products, only CERES FOVs common to both are considered in this study.

## 3. Results

### *a. TOA flux consistency with viewing geometry*

One approach for identifying potential biases in the radiance-to-flux conversion is to examine whether large ensemble averages (i.e., several months) of all-sky (i.e., clear and cloudy) ADM-derived TOA fluxes exhibit any dependence upon viewing geometry. For a given solar zenith angle, average all-sky TOA fluxes should be independent of satellite viewing geometry because TOA flux is not a function of observation angle. This test has previously been used by Payette (1989) and Suttles et al. (1992) with ERBE TOA SW and LW fluxes. They found a 10% relative increase in ERBE TOA albedo with increasing viewing zenith angle and a 6%–7% relative decrease in LW TOA flux with increasing viewing zenith angle. These biases were attributed to ''limitations'' in the ERBE anisotropic models (Suttles et al. 1992). Loeb et al. (2000) performed a similar analysis using ADMs determined from the Polarization and Directionality of Earth Reflectances (POLDER) measurements for scene types identified with POLDER-based cloud property retrievals. In that analysis, albedos showed a much smaller dependence on viewing geometry than for the earlier ERBE results.

Figures 1a and 1b show the 9-month average all-sky

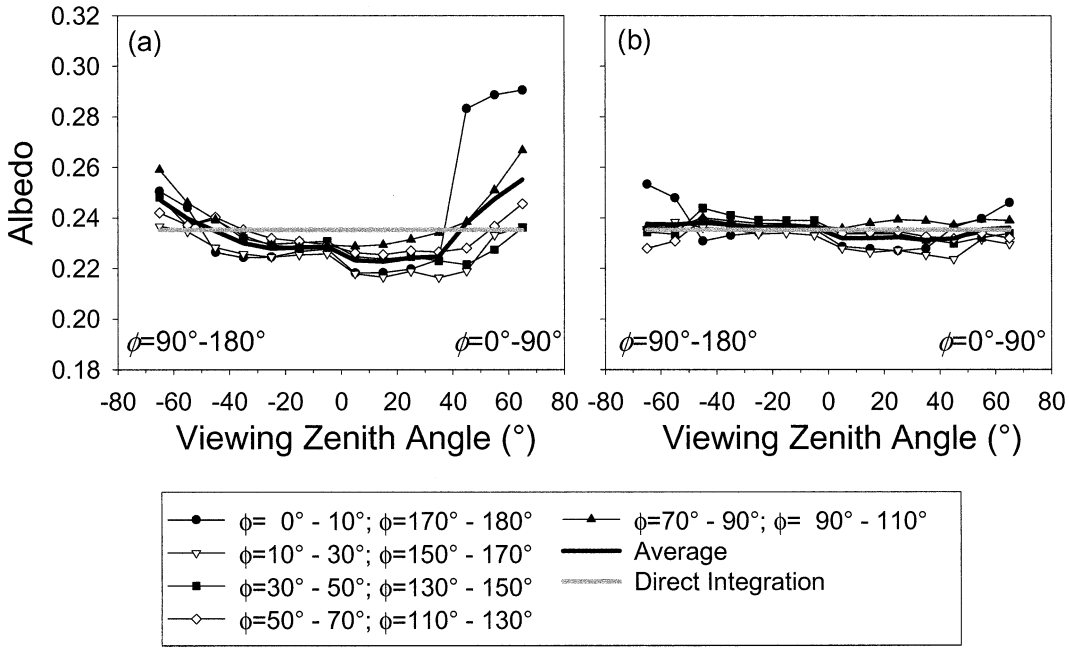


FIG. 1. (a) ERBE-like and (b) CERES SSF mean all-sky TOA albedos for $\theta_0$ = 40°–50° as a function of viewing zenith angle and relative azimuth angle.

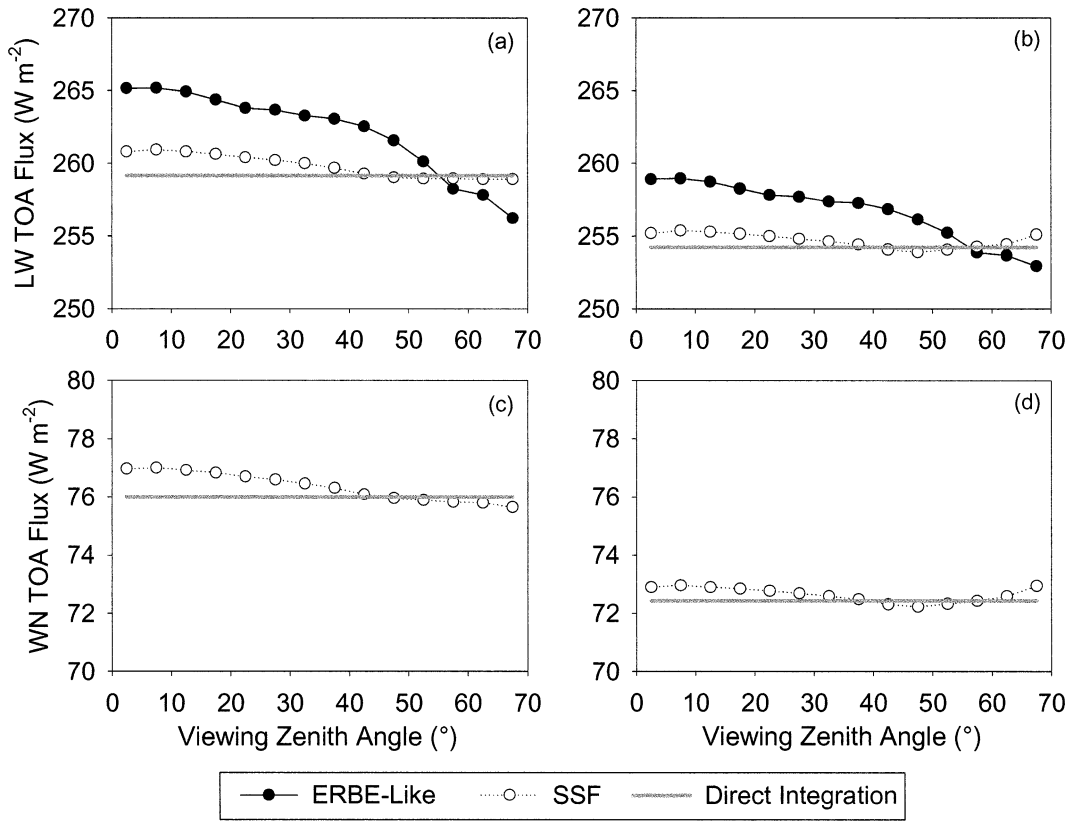


FIG. 2. All-sky mean TOA flux as a function of viewing zenith angle for (a) daytime LW, (b) nighttime LW, (c) daytime WN, and (d) nighttime WN.

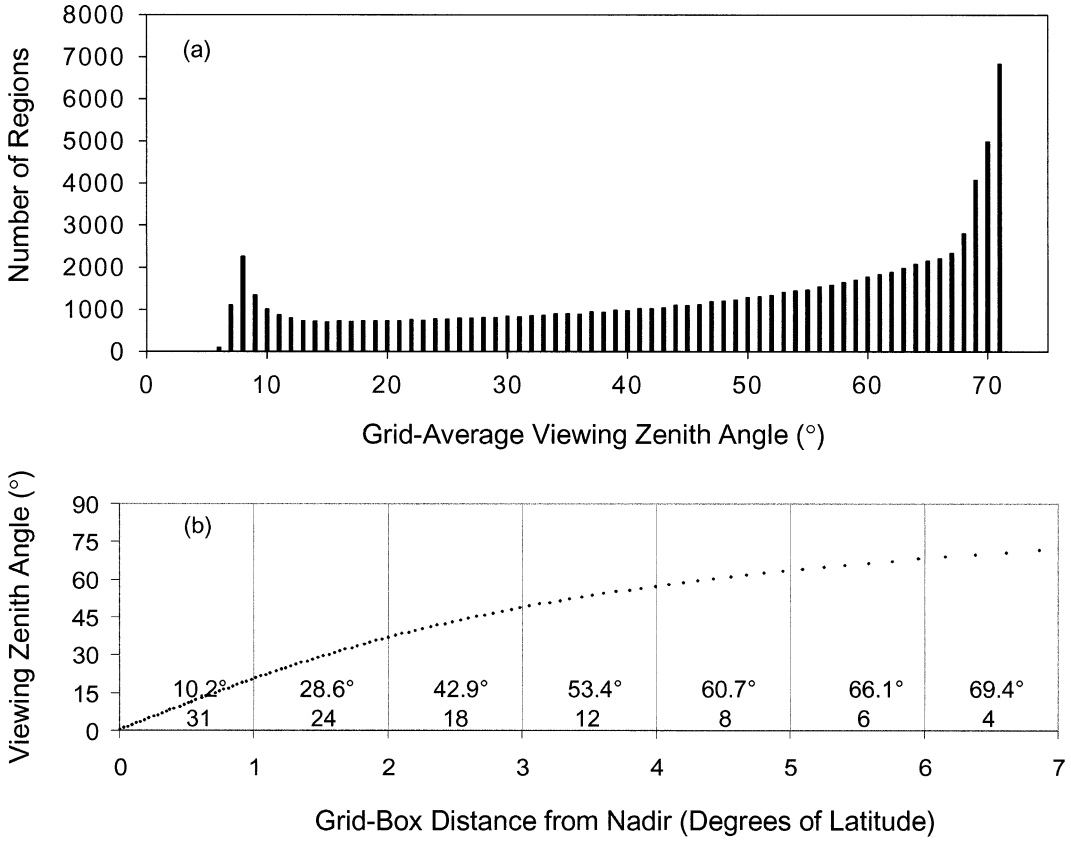


FIG. 3. (a) Distribution of 1° daily grid-averaged viewing zenith angles from 1 month of CERES measurements. (b) Example of CERES FOV sampling by grid-box distance from nadir and viewing zenith angle for one CERES cross-track scan. Numbers correspond to the (top) mean viewing zenith angle and (bottom) number of FOVs in each grid box.

ERBE-like and SSF TOA albedos stratified by CERES viewing zenith angle and relative azimuth angle for solar zenith angles ($\theta_0$) between 40° and 50°. The direct integration albedo (gray line) is determined by sorting CERES radiances between 38°S and 38°N into discrete angular bins defined by the sun–Earth–satellite viewing geometry, averaging the radiances in each angular bin, and integrating the radiances over all angles to produce a TOA flux [Eq. (4) in Loeb et al. 2003]. A TOA albedo is obtained by normalizing the TOA flux by the incident solar irradiance. Because the direct integration method determines TOA albedo directly from measurements without the need for scene identification or angular modeling, it provides a powerful check on the accuracy of averaged ADM-derived TOA albedos.

The ERBE-like albedos (Fig. 1a) show a systematic relative increase of 10% from nadir to the limb, consistent with the earlier results of Payette (1989) and Suttles et al. (1992). TOA albedos are underestimated close to nadir and overestimated at large viewing zenith angles. In contrast, CERES SSF albedos show little dependence on viewing geometry and generally remain within a few percent of the albedo determined by direct integration. Similar results are obtained at other solar zenith angles (not shown).

In the LW, both the CERES SSF and ERBE-like all-sky TOA fluxes decrease with viewing zenith angle (Fig. 2). The ERBE-like all-sky TOA flux decreases by 3.5% (or 9 W m$^{-2}$), as compared with 0.7% ($<$2 W m$^{-2}$) for the SSF TOA flux. Because CERES SSF WN ADMs are based on the same scene-type stratification as the LW ADMs, TOA WN fluxes show a similar dependence on viewing zenith angle as in the LW. Note that because the ERBE-like product does not provide TOA WN fluxes, only CERES SSF WN fluxes are shown in Figs. 2c and 2d.

### *b. Regional mean TOA flux comparison with direct integration*

The three main sources of error in gridded time-averaged TOA fluxes are calibration, angular sampling (i.e., radiance-to-flux conversion), and time sampling. Based on several previous studies of *Nimbus-7* and ERBE data, as well as improvements in CERES measurement strategy, Wielicki et al. (1995) predicted that

TABLE 1. Mean regional SW and LW TOA flux bias (Δ) and rms errors (W m$^{-2}$) for ERBE-like and SSF TOA fluxes as a function of viewing zenith angle range.

| | ERBE-like | | SSF | |
|---|---|---|---|---|
| $\theta$ range | Δ | Rms | Δ | Rms |
| | | SW | | |
| $\theta < 50°$ | −2.73 | 3.12 | 0.03 | 1.42 |
| $\theta < 70°$ | 0.43 | 0.82 | −0.06 | 0.51 |
| | | LW | | |
| $\theta < 50°$ | 4.35 | 4.60 | 0.897 | 1.62 |
| $\theta < 70°$ | 1.22 | 1.33 | 0.29 | 0.49 |

the overall error in CERES monthly regional TOA flux would be ≈2.5 W m$^{-2}$ in the SW and ≈2.5 W m$^{-2}$ in the LW. They estimated that calibration uncertainty would account for ≈1 W m$^{-2}$, angular sampling would account for 0.5–1.0 W m$^{-2}$, and temporal sampling would account for 1–2 W m$^{-2}$.

In order to isolate the angular sampling, or ADM, error contribution, we compare ADM-derived all-sky TOA fluxes with TOA fluxes obtained by direct integration of the measured radiances on a region-by-region basis. TOA fluxes from the direct integration method are obtained in the same manner as in section 3a, but for specific regions rather than for 38°S–38°N. Because only 9 months of CERES TRMM cross-track, RAP, and alongtrack measurements are available, and because the direct integration approach requires CERES radiances over a wide range of viewing zenith angle and relative azimuth angle, the regions must be large enough to ensure adequate angular sampling. Based on sensitivity tests, region sizes of 20° latitude × 20° longitude in the SW and 10° latitude × 10° longitude regions in the LW were found to provide adequate sampling over most CERES TRMM angular bins. For angular bins where measurements are missing, the strategy for filling in angular bins described in section 4 of Loeb et al. (2003) is used.

To determine the regional mean ADM-derived TOA fluxes, instantaneous TOA flux estimates are first averaged into discrete angular bins in each region. Next, the difference between ADM and direct integration TOA fluxes are determined from the following:

$$\Delta F^{\mathrm{SW}}(\theta_{0i};\, \Theta_p,\, \Phi_q) = \left[\frac{1}{n_l}\frac{1}{n_k}\sum_{l=1}^{n_l}\sum_{k=1}^{n_k} \overline{F}^{\mathrm{SW}}_{\mathrm{ADM}}(\theta_{0i},\, \theta_k,\, \phi_l;\, \Theta_p,\, \Phi_q)\chi_k\right] - F^{\mathrm{SW}}_{\mathrm{DI}}(\theta_{0i};\, \Theta_p,\, \Phi_q) \quad \text{and} \tag{1}$$

$$\Delta F^{\mathrm{LW}}(\Theta_p,\, \Phi_q) = \left[\frac{1}{n_k}\sum_{k=1}^{n_k} \overline{F}^{\mathrm{LW}}_{\mathrm{ADM}}(\theta_k;\, \Theta_p,\, \Phi_q)\chi_k\right] - F^{\mathrm{LW}}_{\mathrm{DI}}(\Theta_p,\, \Phi_q), \tag{2}$$

where $\overline{F}^{\mathrm{SW}}_{\mathrm{ADM}}(\theta_{0i},\, \theta_k,\, \phi_l;\, \Theta_p,\, \Phi_q)$ and $\overline{F}^{\mathrm{LW}}_{\mathrm{ADM}}(\theta_k;\, \Theta_p,\, \Phi_q)$ are the mean SW and LW ADM-derived TOA fluxes for latitude–longitude region $(\Theta_p, \Phi_q)$, $F^{\mathrm{SW}}_{\mathrm{DI}}(\theta_{0i};\, \Theta_p,\, \Phi_q)$ and $F^{\mathrm{LW}}_{\mathrm{DI}}(\Theta_p,\, \Phi_q)$ are the SW and LW direct integration TOA fluxes, respectively, and $n_k$ and $n_l$ are the number of viewing zenith and relative azimuth angle bins, respectively. Here, $(\theta_{0i},\, \theta_k,\, \phi_l)$ corresponds to the midpoint of a discrete angular bin defined by $(\theta_{0i} \pm \Delta\theta_0/2,\, \theta_k \pm \Delta\theta/2,\, \phi_l \pm \Delta\phi/2)$, where $\Delta\theta_0$, $\Delta\theta$, and $\Delta\phi$ represent the angular bin resolution (see Fig. 3 of Loeb et al. 2003), $\chi_k$ is a normalized weighting factor that accounts for the viewing zenith angle sampling over a 1° grid box within the 10° and 20° comparison regions. The 1° grid-box size corresponds to the nominal resolution of CERES monthly mean regional TOA flux products. The factor $\chi_k$ is derived from the distribution of daily grid-averaged viewing zenith angles for 1 month of cross-track CERES ERBE-like measurements (Fig. 3a). The shape of the $\chi_k$ distribution is mainly due to geometry. Because of the earth's curvature, and because CERES collects data in the alongscan direction at a fixed rate, the separation distance between consecutive FOVs increases with viewing zenith angle (Fig. 3b). The increased spacing between consecutive footprints means that 1° regions observed from large viewing zenith angles will see fewer FOVs, but these FOVs will cover a larger area. Consequently, the frequency of occurrence of daily-averaged viewing zenith angle at the 1° scale peaks at larger viewing zenith angles.

Because the TRMM spacecraft is in a precessing orbit with a 46-day repeat cycle, each solar zenith angle bin $\theta_{0i}$ in Eq. (1) is sampled in every region at least 5 times over the 9 months of CERES TRMM measurements. To estimate the monthly regional SW TOA flux bias, $\Delta F^{\mathrm{SW}}(\theta_{0i};\, \Theta_p,\, \Phi_q)$ values from each region are temporally averaged over 1 month as follows:

$$\Delta F^{\mathrm{SW}}(\Theta_p,\, \Phi_q)\,\frac{1}{n_d}\frac{1}{n_t}\sum_{l=1}^{n_d}\sum_{k=1}^{n_t} \Delta F^{\mathrm{SW}}[\theta_{0i}(d_l,\, t_k);\, \Theta_p,\, \Phi_q], \tag{3}$$

where $n_d$ is the number of days in a month, $n_t$ is the number of time steps used to determine a 24-h average flux bias, and $\theta_{0i}(d_l,\, t_k)$ is the midpoint of the CERES solar zenith angle bin corresponding to the solar zenith angle at time $t_k$ on day $d_l$. To evaluate Eq. (3), the solar zenith angle sampling for the month of March 1998 is used with 144 ten-minute time steps.

Regional SW TOA flux bias errors are shown in Figs. 4a–d and summarized in Table 1 for both CERES ERBE-like and SSF TOA fluxes. Separate analyses are performed for two viewing zenith angle ranges: nadir to 50° and nadir to 70°. In the CERES TRMM SSF product, CERES footprints are retained only when they partially lie within the VIRS imager swath, which has a maximum viewing zenith angle of 49°. Therefore, the 50° viewing zenith angle cutoff is representative of the angular sampling when CERES is in a cross-track scan mode, and the 70° cutoff is representative of angular

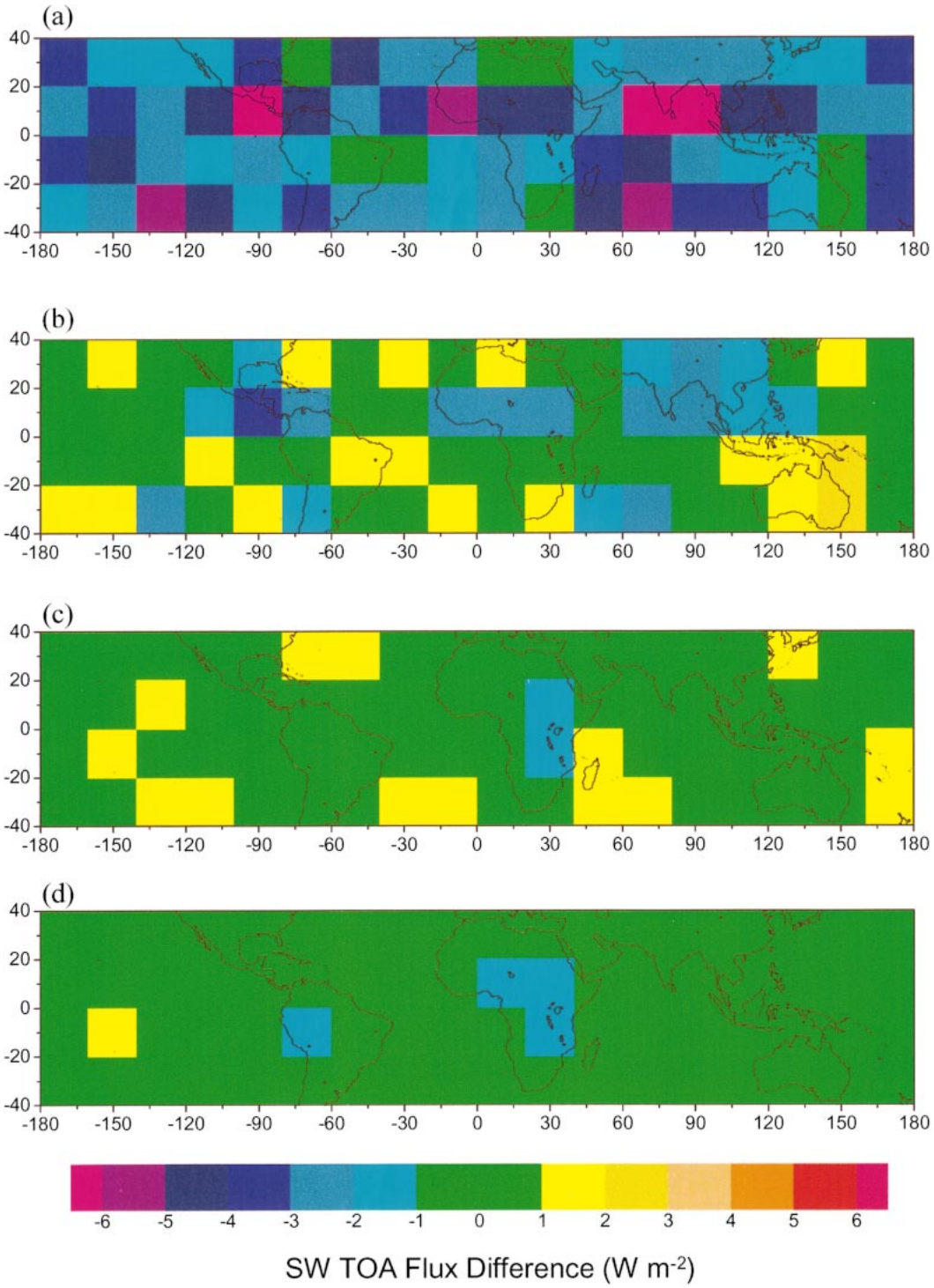


FIG. 4. Error in 1° monthly mean all-sky SW TOA flux inferred from the difference between ADM-derived TOA fluxes and TOA fluxes obtained by direct integration of measured radiances. Differences are diurnally averaged using the solar zenith angle sampling from Mar 1998: (a) ERBE-like for viewing zenith angles between 0° and 50°, (b) SSF for viewing zenith angles between 0° and 50°, (c) ERBE-like for viewing zenith angles between 0° and 70°, and (d) SSF for viewing zenith angles between 0° and 70°.

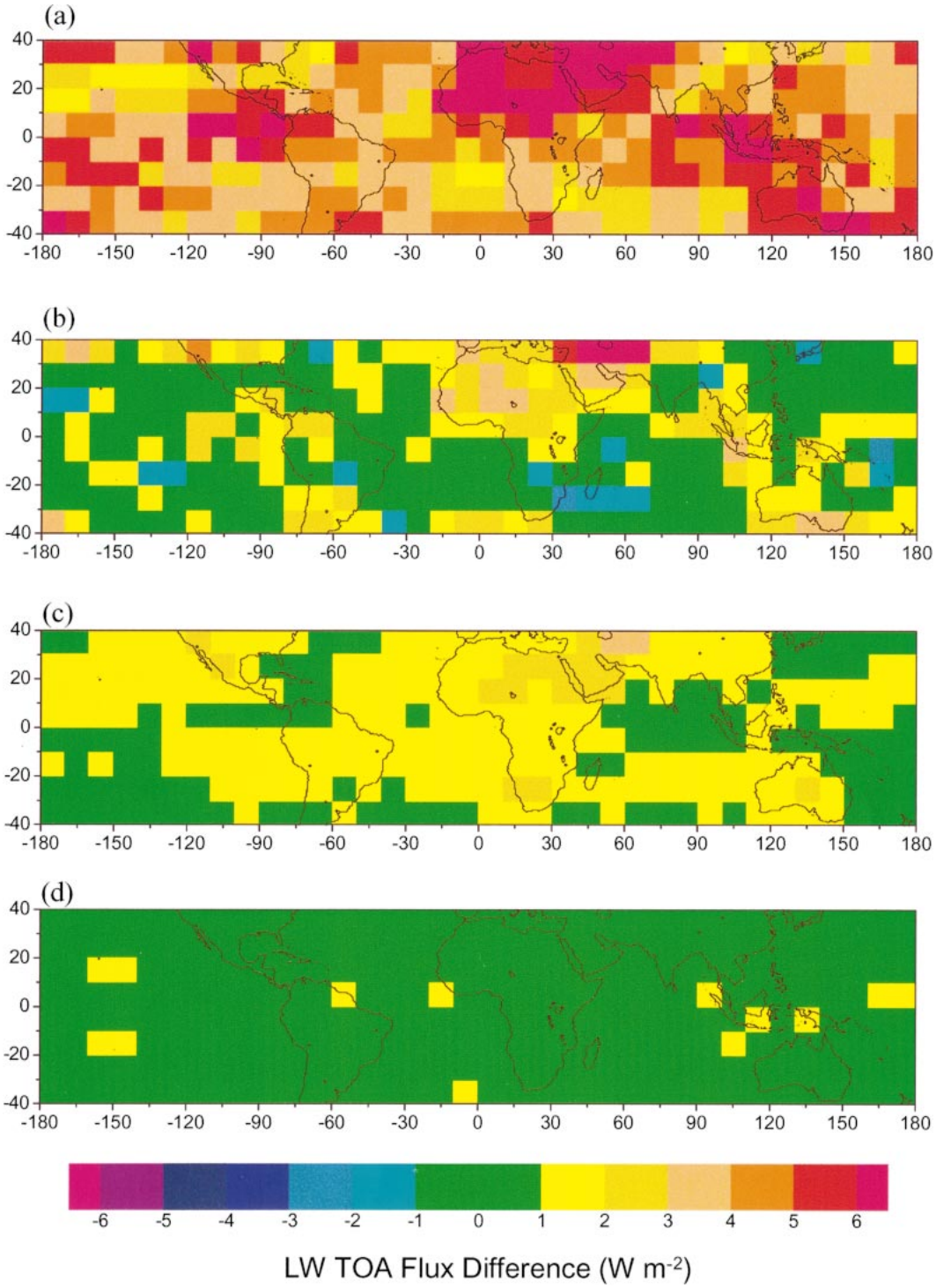


FIG. 5. Error in 1° monthly mean all-sky LW TOA flux inferred from the difference between ADM-derived TOA fluxes and TOA fluxes obtained by direct integration of measured radiances: (a) ERBE-like for viewing zenith angles between 0° and 50°, (b) SSF for viewing zenith angles between 0° and 50°, (c) ERBE-like for viewing zenith angles between 0° and 70°, and (d) SSF for viewing zenith angles between 0° and 70°.

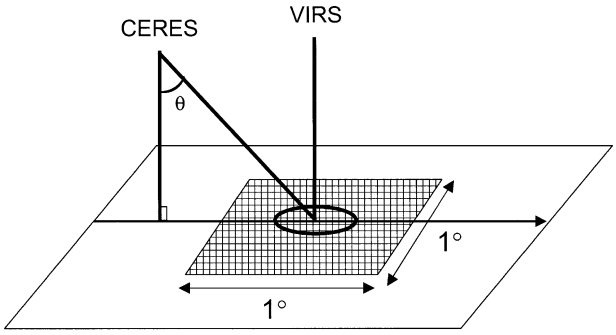


FIG. 6. Schematic of CERES and VIRS viewing geometries for regional instantaneous TOA flux consistency tests.

sampling in the SSF product when CERES is in a RAP scan mode (radiance-to-flux conversion is not performed when $\theta > 70°$). In RAP mode, CERES footprints at viewing zenith angles $>49°$ appear in the SSF product when the angle between the CERES scan plane and the satellite orbital plane is less than 90°.

Over most of the Tropics, the ERBE-like SW TOA fluxes for the nadir to 50° viewing zenith angle range (Fig. 4a) are smaller than SW TOA fluxes evaluated by direct integration. The average TOA flux bias error is $-2.7$ W m$^{-2}$. In contrast, both positive and negative bias errors are observed for the CERES SSF SW TOA fluxes (Fig. 4b), and the bias over the entire Tropics is close to zero. The root-mean-square (rms) error in the SSF regional mean SW TOA flux is 1.4 W m$^{-2}$, which is larger than the 0.5–1.0 W m$^{-2}$ error predicted by Wielicki et al. (1995). When viewing zenith angles from nadir to 70° are considered, the ERBE-like SW TOA flux bias error (Fig. 4c) is 0.43 W m$^{-2}$. This reduction in bias error is due to error compensation at large and small viewing zenith angles. The CERES SSF SW TOA flux bias error (Fig. 4d) remains close to zero and the rms error in the regional mean TOA flux is now 0.51 W m$^{-2}$, which is well within the range predicted by Wielicki et al. (1995).

In the LW, the ERBE-like product overestimates LW TOA fluxes for viewing zenith angles between nadir and 50° (Fig. 5a). The average LW flux bias is 4.4 W m$^{-2}$, as compared with 0.87 W m$^{-2}$ for the SSF (Fig. 5b). For viewing zenith angles between nadir and 70°, the ERBE-like TOA flux bias is 1.2 W m$^{-2}$ (Fig. 5c), compared to 0.29 W m$^{-2}$ for the SSF results. The rms error in the SSF regional mean LW TOA flux for viewing zenith angles $<70°$ is 0.49 W m$^{-2}$, which is also

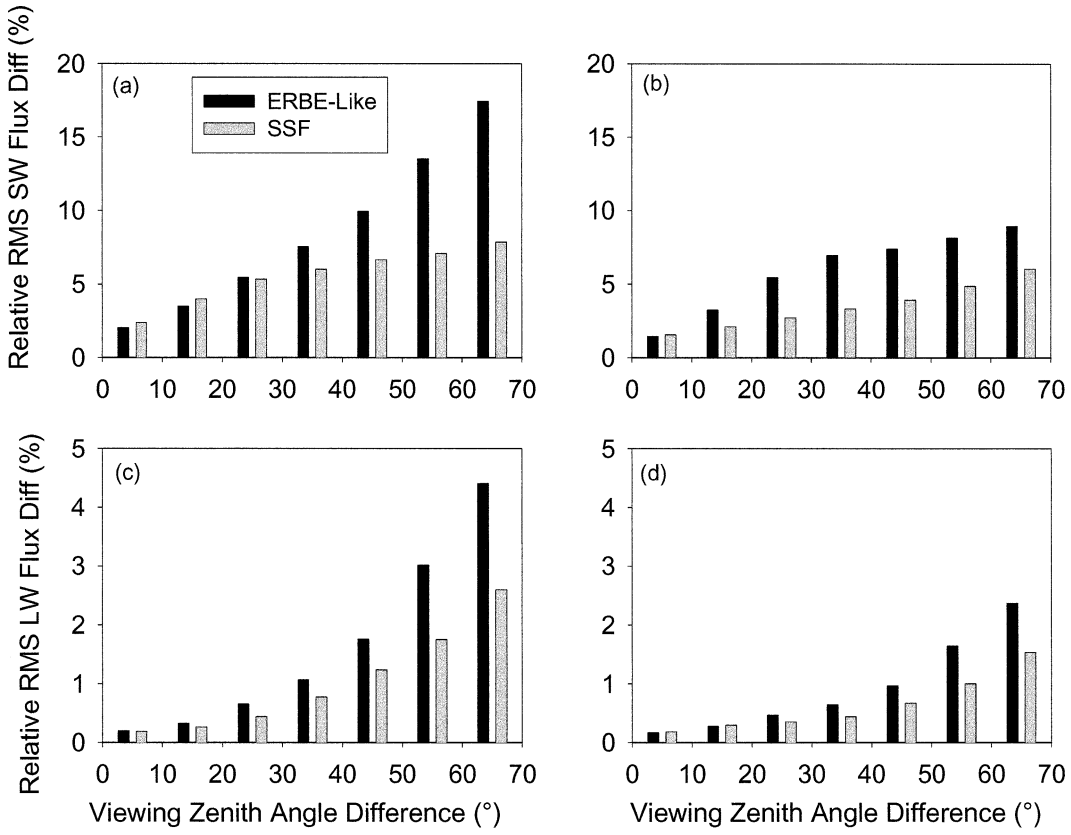


FIG. 7. Relative rms difference between TOA fluxes determined from VIRS nadir radiances and off-nadir CERES measurements as a function of the viewing zenith angle separation for (a) all-sky SW TOA fluxes, (b) clear-sky SW TOA fluxes, (c) all-sky LW TOA fluxes, and (d) clear-sky LW TOA fluxes.

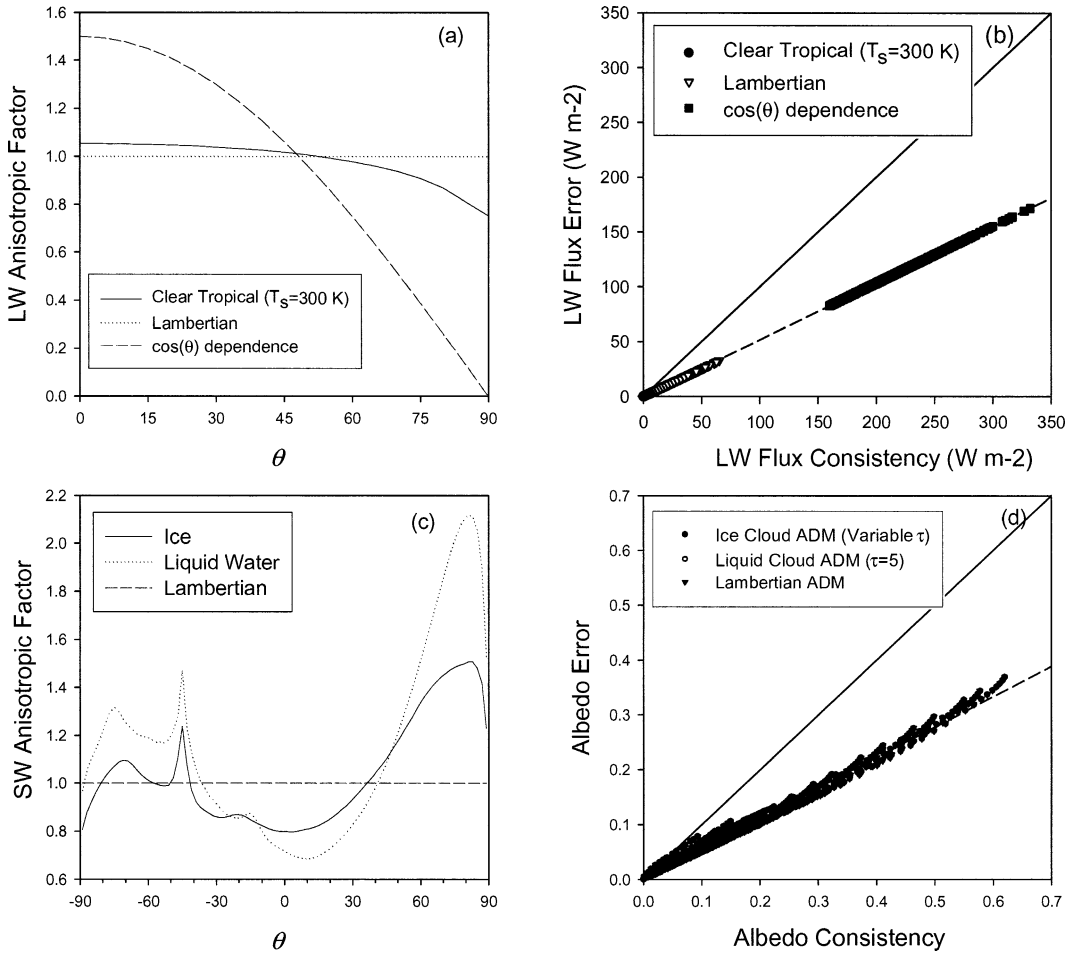


FIG. 8. (a) LW anisotropic factors against viewing zenith angle for three assumed ADMs, (b) LW flux error against LW flux consistency, (c) SW anisotropic factor against viewing zenith angle for three assumed ADMs, and (d) albedo error against albedo consistency for three assumed ADMs.

within the 0.5 W $m^{-2}$ accuracy predicted by Wielicki et al. (1995).

### *c. Regional instantaneous TOA flux consistency test*

Because scanning radiometers can only measure TOA radiances from a limited number of directions over a scene at any one time, it is not possible to use an approach like the direct integration method to validate instantaneous ADM-derived TOA fluxes. However, because the actual TOA flux is independent of satellite viewing geometry, a powerful consistency check is to compare instantaneous TOA fluxes estimated from multiangle measurements over the same scene. If the TOA flux estimates from different angles are not the same, this indicates that the anisotropy of the scene is poorly characterized by the ADM. Conversely, if the TOA flux estimates are the same, this provides some confidence that the anisotropy of the scene is modeled correctly. Note, however, that ''consistency'' is not a guarantee of absolute accuracy because it does not account for potential bias errors that are independent of viewing geometry.

TABLE 2. Estimated regional instantaneous SW and LW TOA flux errors (W $m^{-2}$) in all-sky and clear-sky conditions.

| | All-sky | | Clear-sky | |
|---|---|---|---|---|
| Channel | ERBE-like | SSF | ERBE-like | SSF |
| SW | 24.4 | 10.8 | 12.3 | 8.7 |
| LW | 5.8 | 3.5 | 3.7 | 2.4 |

While it might be tempting to compare instantaneous TOA fluxes inferred from different CERES angles directly, this approach is limited because spatial matching errors dominate the comparison. Because the CERES FOV shape and size change with viewing zenith angle, part of the area observed from oblique viewing zenith angles will not be seen by collocated FOVs at near-nadir angles. Furthermore, because the CERES along-track scan is aligned with the satellite ground track, and

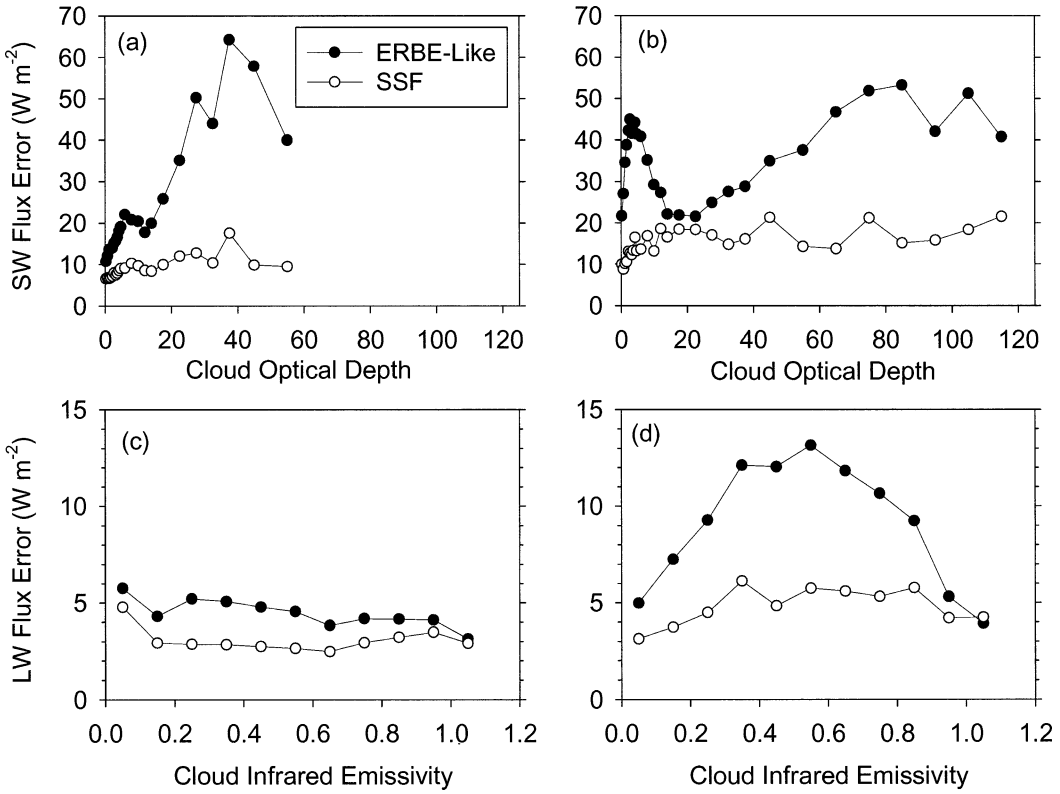


FIG. 9. Estimated SSF and ERBE-like instantaneous SW TOA flux errors for (a) liquid water and (b) ice clouds as a function of cloud optical depth; LW TOA flux errors for (c) liquid water and (d) ice clouds as a function of cloud infrared emissivity.

because the earth rotates during the time interval between oblique and nadir views of a point along the ground track, it not possible to spatially average consecutive nadir footprints to match the area observed at oblique angles because the earth locations corresponding to the nadir and oblique angles will be displaced from one another.

To avoid this, we take advantage of the fact that CERES processing carefully collocates VIRS pixels within a CERES FOV. When CERES scans in the alongtrack scan mode, it acquires measurements from limb to limb along the satellite ground track. The VIRS imager observes the same area as CERES within approximately 2 min, but from viewing zenith angles close to nadir (Fig. 6) either before or after CERES. In order to take advantage of the close VIRS–CERES spatial and temporal coincidence, TOA fluxes from CERES are compared with broadband TOA fluxes estimated from collocated VIRS narrowband (nadir) radiances. To optimize spatial matching between CERES and VIRS measurements, VIRS pixels within CERES FOVs are weighted by the CERES point spread function (PSF) (Smith 1994). The matching is done sufficiently close to ensure an instantaneous matching noise of less than 1.5% in visible channel radiances and less than 0.5% in infrared radiances. A VIRS 0.63-$\mu$m radiance average over a CERES footprint is converted to a broadband radiance by applying a narrow-to-broadband correction derived from a linear fit between all coincident nadir CERES and VIRS radiances within a 1° latitude–longitude region. The VIRS broadband radiances are then converted to TOA fluxes in the same manner as CERES radiances (Loeb et al. 2003). Consequently, the main error sources in the CERES–VIRS TOA flux comparison are ADM errors and narrow-to-broadband conversion errors. To minimize narrow-to-broadband conversion errors, only 1° regions where the rms error in the narrow-to-broadband fit is smaller than 5% are considered in the analysis. This occurs for approximately 72% of the regions in both all-sky and clear-sky conditions. To further reduce the influence of instantaneous errors in the narrow-to-broadband conversion, we average the CERES- and VIRS-derived TOA fluxes in each 1° region. Based on a separate analysis of TOA fluxes from the two CERES instruments on the *Terra* spacecraft, the relative error in TOA flux introduced by the narrow-to-broadband conversion is estimated to be 1.61% in the SW and 1.54% in the LW.

Figures 7a–d show the consistency between TOA fluxes from VIRS nadir and CERES off-nadir radiance measurements from 9 alongtrack scan days. All-sky results are based upon 13 259 1° regions, and results for

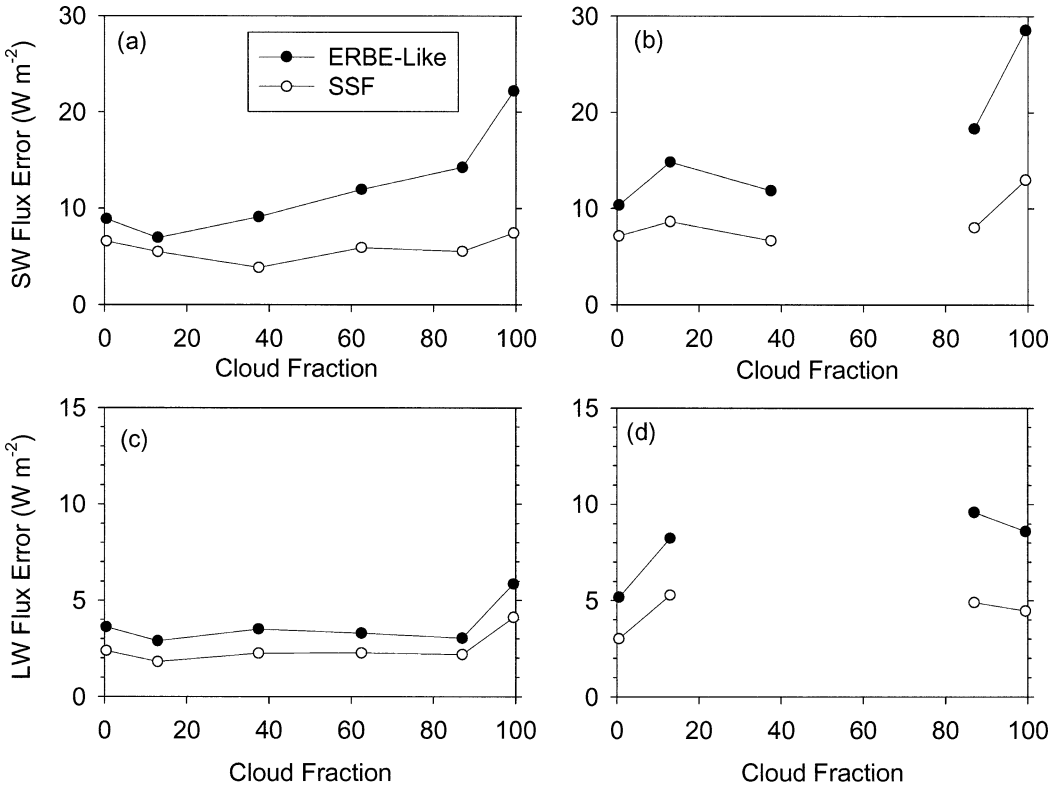


FIG. 10. Estimated SSF and ERBE-like instantaneous SW TOA flux errors as a function of cloud fraction for (a) liquid water and (b) ice clouds; LW TOA flux errors as a function of cloud fraction for (c) liquid water and (d) ice clouds.

cloud-free conditions (as identified from VIRS) are based upon 1701 1° regions. TOA flux consistency is determined from the rms difference between VIRS and CERES TOA fluxes. In all cases TOA flux rms differences increase with increasing CERES and VIRS viewing zenith angle difference. The increase is more pronounced in the ERBE-like results. When the VIRS and CERES viewing zenith angle separation is between 60° and 70°, the relative rms difference (defined as the VIRS–CERES TOA flux rms difference divided by the mean TOA flux) in all-sky SW TOA flux is a factor of 2.2 smaller for the SSF result than the ERBE-like result. In the LW, the SSF-relative rms differences are reduced by a factor of 1.55, in comparison with ERBE. Under cloud-free conditions the SSF-relative rms differences are smaller by factors of 1.45 and 1.55 in the SW and LW, respectively.

Because the true instantaneous TOA flux for a CERES FOV is unavailable, there is no direct way of determining the actual instantaneous TOA flux error. However, because TOA flux consistency and TOA flux error are closely related, it is possible to provide an indirect estimate of TOA flux error. To determine the relationship between TOA flux consistency and ''true'' flux error, ADM simulations are performed using radiances generated from a broadband 1D radiative transfer model. For each scene, the TOA flux consistency between nadir and off-nadir viewing zenith angles is compared with the corresponding TOA flux error. Figure 8a shows three assumed LW ADMs: (i) an ADM for a clear tropical atmosphere with surface temperature of 300 K computed from the moderate-resolution transmittance (MODTRAN) (Berk et al. 1999) radiative transfer model, (ii) a Lambertian ADM, and (iii) an ADM derived from radiances that have a $\cos\theta$ dependence on viewing zenith angle. Each assumed ADM is applied to a population of theoretical LW radiances generated from MODTRAN for different clear and cloudy conditions. Next, the total flux error at nadir and $\theta = 65°$ is plotted as a function of the TOA flux consistency, regardless of the ADM used. The result, provided in Fig. 8b, shows that TOA flux error is approximately half as large as TOA flux consistency. In the SW, three assumed ADMs are used to estimate albedos from radiances computed for liquid water clouds with optical depths between 0.1 and 200. The 1D radiative transfer model of Nakajima and Tanaka (1986) is used to generate the radiances. The assumed ADMs are (i) an ice cloud ADM (from theory) with variable cloud optical depths, (ii) a liquid water cloud ADM (from theory) with a fixed cloud optical depth of 5, and (iii) a Lambertian ADM. Figure 8c shows an example of the three ADMs at a solar zenith angle of 45° in the principal plane, and Fig. 8d provides the albedo error and consistency results. Each point in

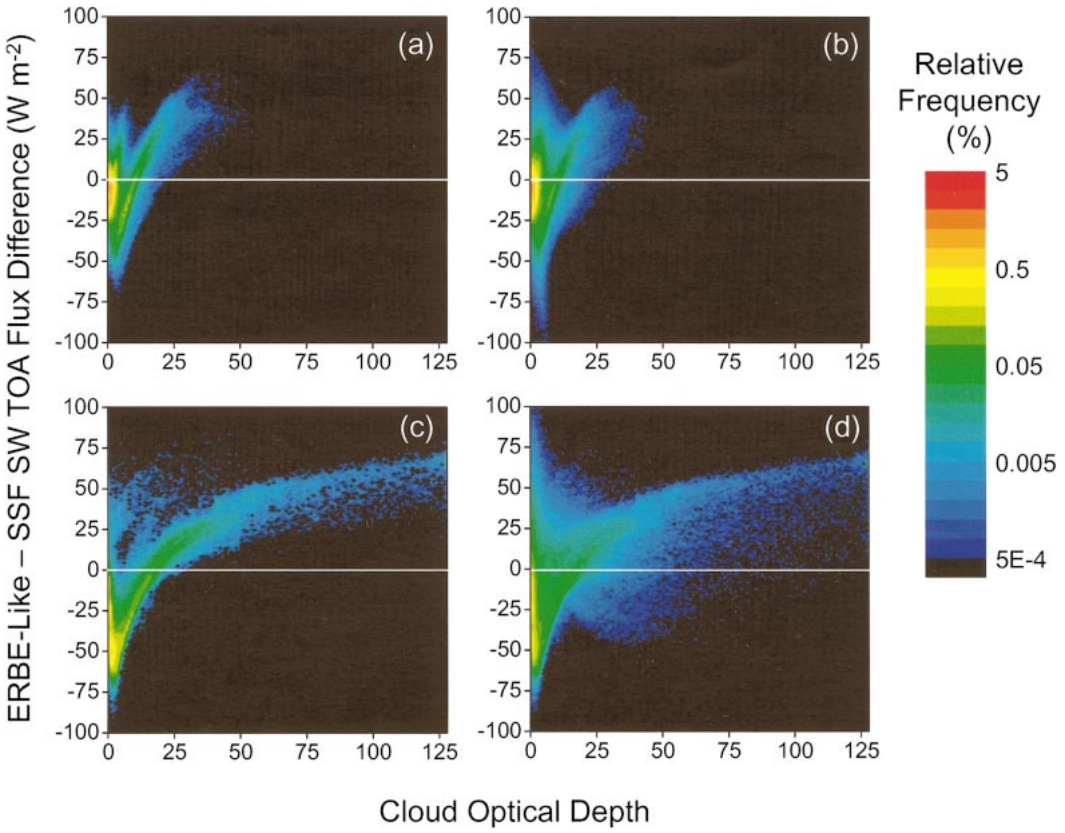


FIG. 11. Difference between CERES ERBE-like and CERES SSF SW TOA flux (ERBE-like minus SSF) against cloud optical depth for liquid water clouds when (a) $\theta \leq 25°$ and (b) $\theta \leq 70°$, and for ice clouds when (c) $\theta \leq 25°$ and (d) $\theta \leq 70°$. The solar zenith angle range is 42°–44°.

Fig. 8d corresponds to a specific solar zenith angle and cloud optical depth. TOA albedo consistency for a given solar zenith angle and cloud optical depth is obtained from the rms difference between albedos at nadir and $\theta = 65°$ for 90 relative azimuth angles between 0° and 180°. The correlation between TOA albedo error and consistency is 0.991, and TOA albedo error is approximately 55% of the TOA albedo consistency.

Table 2 summarizes the estimated TOA flux errors obtained when the above approximate relationships between TOA flux error and TOA flux consistency are applied to the CERES results in Fig. 7. To be consistent with Wielicki et al. (1995), the SW TOA flux errors are defined for a TOA solar irradiance of 1000 W m$^{-2}$ (i.e., a solar zenith angle of 42.895°). SSF all-sky SW and LW TOA flux errors are 10.8 and 3.5 W m$^{-2}$, respectively.

Figures 9a–d show TOA flux errors as a function of cloud optical depth and cloud infrared emissivity for liquid water and ice clouds. Cloud optical depths and cloud infrared emissivities are determined by averaging individual footprint-level values within each 1° region. In the SW, SSF TOA flux errors are generally less than 20 W m$^{-2}$ and show little dependence on cloud optical depth. In contrast, ERBE-like TOA flux errors are a factor of 2–5 larger (reaching 65 W m$^{-2}$), and depend strongly on cloud optical depth. The largest improvements in TOA flux accuracy from the SSF ADMs occur for thin ice and thick liquid water clouds. In the LW, SSF TOA flux errors are generally a factor of 1.5–2.0 smaller than the ERBE-like errors. The largest errors in both SSF and ERBE-like TOA LW fluxes occur for ice cloud infrared emissivities between 0.5 and 0.7, where SSF TOA flux errors reach 6 W m$^{-2}$ and ERBE-like TOA flux errors reach 13 W m$^{-2}$. Similar results are obtained when the errors are stratified by cloud fraction, as shown in Figs. 10a–d. Note that the gaps in Figs. 10b and 10d for the ice cloud cases are due to inadequate sampling.

### *d. CERES SSF and ERBE-like TOA flux differences by cloud type*

One of the advances of the new CERES TRMM SSF ADMs over ERBE is improved sensitivity to parameters that influence the anisotropy of the observed scenes. To examine the difference between CERES SSF and ERBE-like instantaneous TOA fluxes, Figs. 11 and 12 show SW (for $\theta_0 = 42°$–44°) and LW TOA flux differences (ERBE-like minus SSF) stratified by

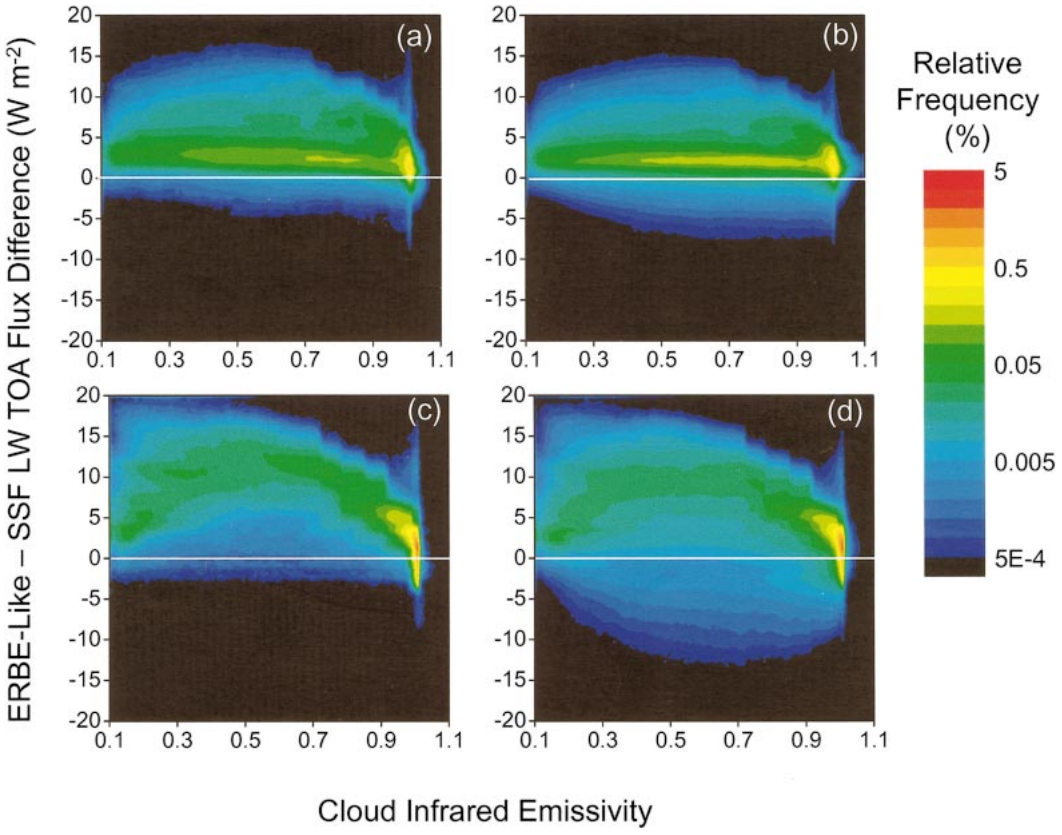


FIG. 12. Difference between CERES ERBE-like and CERES SSF LW TOA flux (ERBE-like minus SSF) against cloud infrared emissivity for liquid water clouds when (a) $\theta \leq 25°$ and (b) $\theta \leq 70°$, and for ice clouds when (c) $\theta \leq 25°$ and (d) $\theta \leq 70°$.

cloud phase, cloud optical depth, and cloud infrared emissivity. Because ERBE-like SW ADMs underestimate (overestimate) the anisotropy of thin (thick) clouds (Loeb et al. 2003), SW TOA flux differences for $\theta < 25°$ (Figs. 11a and 11c) are negative for thin clouds and positive for thick clouds. When all viewing zenith angles are considered (Figs. 11b and 11d), TOA flux differences show a broader distribution because differences in anisotropy between ERBE and SSF ADMs depend on viewing zenith angle (cf. Fig. 13 of Loeb et al. 2003). In the LW (Fig. 12), TOA flux differences are smaller, but nonetheless depend systematically on cloud infrared emissivity.

### *e. Cloud radiative forcing sensitivity to ADMs, scene identification, and directional models*

For climate studies there often is a need to compare the radiative effects of clouds between different regions or over the same region during different time periods. A metric commonly used to assess the radiative impact of clouds on the climate system is cloud radiative forcing (CRF) (Ramanathan et al. 1989; Harrison et al. 1990), which is defined as the TOA flux difference between clear and all-sky conditions,

$$\text{SW CRF} = F^{\text{SW}} - F^{\text{SW}}_{\text{clr}} \quad \text{and} \tag{4}$$

$$\text{LW CRF} = F^{\text{LW}}_{\text{clr}} - F^{\text{LW}}, \tag{5}$$

where $F^{\text{SW}}$ and $F^{\text{LW}}$ are the all-sky SW and LW diurnally averaged TOA fluxes, respectively, and $F^{\text{SW}}_{\text{clr}}$ and $F^{\text{LW}}_{\text{clr}}$ are the clear-sky SW and LW diurnally averaged TOA fluxes, respectively. To examine how differences between ERBE and SSF ADMs affect regional CRF, we consider two regions with distinct cloud properties, namely, the west (5°S–5°N, 140°–165°E) and east (5°S–5°N, 80°–105°W) tropical Pacific Ocean. Because of their sensitivity to El Niño–Southern Oscillation (ENSO) events, these regions have received a great deal of attention recently (e.g., Wong et al. 2000; Cess et al. 2001; Lindzen et al. 2001; Lin et al. 2002; Chambers et al. 2002). During a non–El Niño year, the west Pacific Ocean region (or warm pool) is dominated by convective clouds, whereas stratiform clouds persist in the east Pacific Ocean region.

To determine the cloud radiative forcing in these two regions, daily-averaged clear and all-sky TOA fluxes are inferred from instantaneous SW and LW TOA fluxes and averaged into 1° latitude–longitude regions. An instantaneous TOA flux is converted to a daily mean

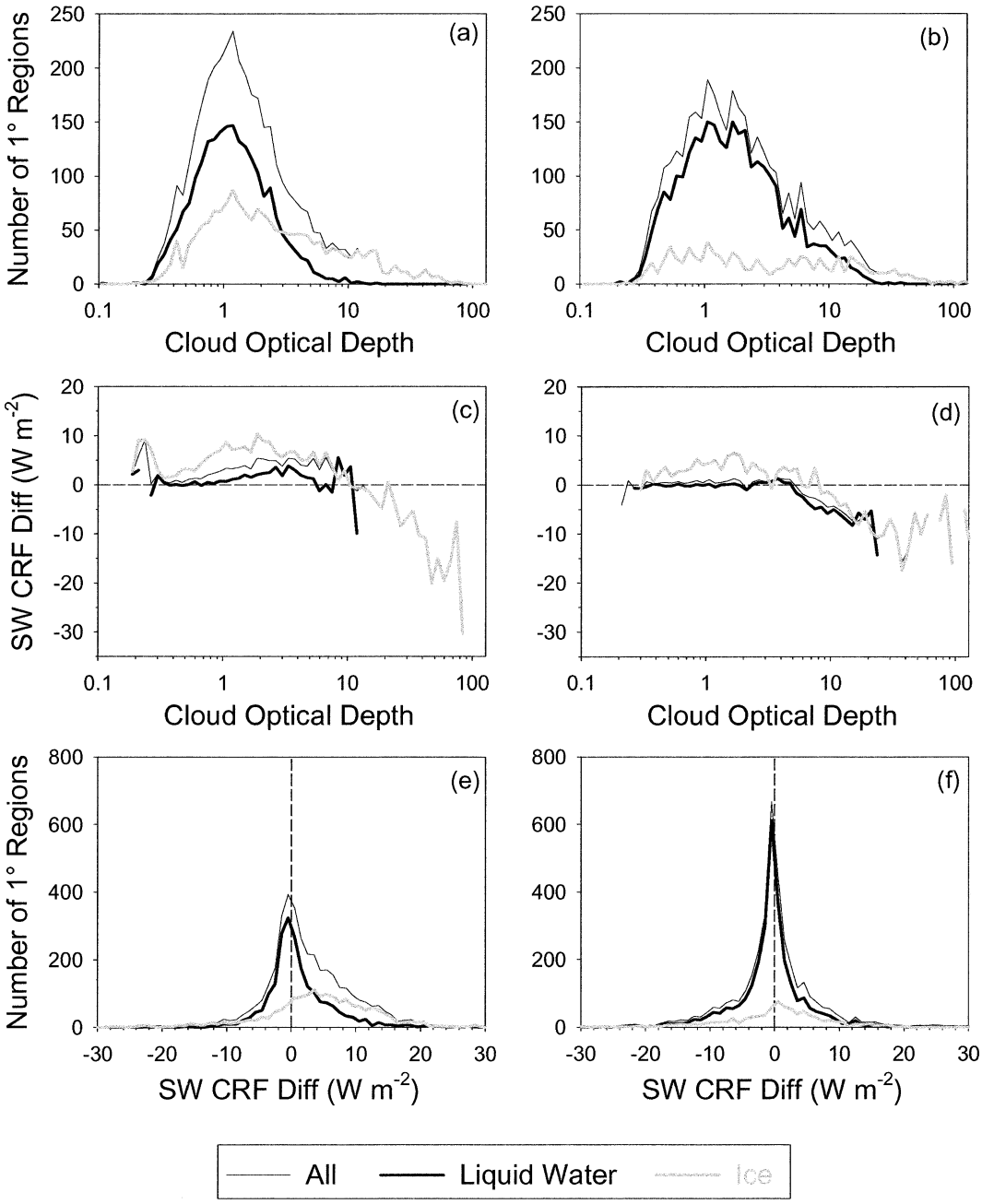


FIG. 13. (a), (b) Distribution of 1° daily mean cloud optical depth, (c), (d) average SW CRF difference (ERBE-like minus SSF) against cloud optical depth, and (e), (f) distribution of 1° SW CRF difference (ERBE-like minus SSF) for the (left) west and (right) east Pacific Ocean regions.

TOA flux by modeling the diurnal variation of albedo using scene-type-dependent directional albedo models (Brooks et al. 1986; Young et al. 1998) derived from the CERES TRMM ADMs. In deriving the daily mean flux from an instantaneous value, the footprint's scene type is assumed to remain constant throughout the day. In order to isolate the influence of ERBE and SSF ADM differences on CRF, the same population of clear scenes (as identified by VIRS) is used to determine both ERBE-like and SSF CRF, and the same directional models (i.e., derived from the CERES TRMM ADMs) are used in both cases to derive daily mean TOA fluxes.

Figures 13a–f compare SW CRF differences between CERES ERBE-like and SSF for the two regions in March 2000. During the entire month, the CERES instrument was in a cross-track scan mode. As a result, only CERES footprints with viewing zenith angles less than 49° are available for this period in the SSF prod-

TABLE 3. TOA fluxes and cloud radiative forcings in the west Pacific Ocean region (5°S–5°N, 140°–165°E) for Mar 2000. ES8 corresponds to the ERBE-like results. Only daytime measurements are considered; $f$ is cloud fraction, $\tau$ is cloud optical depth, $Z_e$ is effective cloud height, and "Count" is the number of 1° regions considered.

| | SW flux (W m$^{-2}$) | | LW flux (W m$^{-2}$) | | SW CRF (W m$^{-2}$) | | LW CRF (W m$^{-2}$) | | Net CRF (W m$^{-2}$) | | $f$ | $\tau$ | $Z_e$ | Count |
|---|---|---|---|---|---|---|---|---|---|---|---|---|---|---|
| | SSF | ES8 | SSF | ES8 | SSF | ES8 | SSF | ES8 | SSF | ES8 | (%) | (−) | (km) | (−) |
| Clear | 40.5 | 38 | 286.5 | 288.4 | — | — | — | — | — | — | — | — | — | — |
| Liquid | 61.8 | 58.4 | 276.1 | 279.6 | −21.3 | −20.4 | 10.4 | 8.8 | −10.9 | −11.6 | 41 | 1.35 | 3.01 | 1925 |
| Ice | 118.8 | 111.9 | 211.2 | 216.7 | −78.3 | −73.9 | 75.3 | 71.7 | −3 | −2.2 | 85 | 2.36 | 8.84 | 1876 |
| All | 89.4 | 84.3 | 244.5 | 249 | −48.9 | −46.3 | 41.9 | 39.3 | −7 | −6.9 | 62 | 1.78 | 5.89 | 3839 |

uct. Based on results in section 3b, these results provide an upper bound on CRF sensitivity to differences between the ERBE and CERES SSF ADMs. The SW CRF differences (ERBE-like minus SSF) are generally larger in the west Pacific Ocean region, as is evident from the broader frequency distributions in Fig. 13e compared to Fig. 13f. A positive (negative) SW CRF difference means the ERBE ADMs produce less (more) SW radiative cooling than the SSF ADMs. Results in Figs. 13c and 13d suggest that the ERBE-like ADMs produce less SW radiative cooling for thin clouds and more SW radiative cooling for thick clouds when compared with the CERES SSF ADMs. For ice clouds, SW CRF differences range from +10 W m$^{-2}$ for clouds of optical depth near 2, to −15 W m$^{-2}$ for clouds with optical depths >35. For liquid water clouds with optical depths <5 SW CRF differences are smallest (<2 W m$^{-2}$). Overall, the ERBE ADMs produce 2.6 W m$^{-2}$ (5.3%) less SW radiative cooling than the SSF ADMs in the west Pacific Ocean region (Table 3), and 0.3 W m$^{-2}$ (0.7%) more SW radiative cooling in the east Pacific Ocean region (Table 4). The rms difference in 1° daily mean SW CRF is 7–8 W m$^{-2}$ (15%).

The LW CRF differences between CERES and ERBE are shown in Figs. 14a–f as a function of cloud infrared emissivity. A positive (negative) LW CRF difference means the ERBE ADMs produce more (less) LW radiative warming than the SSF ADMs. For most cloud conditions, the ERBE-like ADMs produce less LW radiative warming. This is not unexpected given the large positive bias errors in ERBE-like LW TOA fluxes in Figs. 2a and 2b for viewing zenith angles <50°. Differences are more pronounced for ice clouds, reaching −6 W m$^{-2}$ at cloud infrared emissivities between 0.1 and 0.2 in the west Pacific Ocean region (Fig. 14c). In contrast, the largest LW CRF differences in the east Pacific Ocean region occur at cloud infrared emissivities near 0.6 and decrease in magnitude with decreasing cloud infrared emissivity (Fig. 14d). This regional difference is explained by the fact that when clouds with small cloud infrared emissivity occur in the east Pacific Ocean region, their cloud fraction is generally much smaller than in the west Pacific region. This is illustrated in Fig. 15c, which shows the cloud fraction distribution for clouds with cloud infrared emissivity less than 0.5. Because LW CRF decreases with decreasing cloud cover (i.e., as scenes become clearer), LW CRF sensitivity to ADM differences is reduced (Figs. 15a–b). Overall, ERBE ADMs produce ≈2.6 W m$^{-2}$ (6.2%) less LW radiative warming in the west in comparison with SSF ADMs (Table 3), and ≈1.5 W m$^{-2}$ (6.3%) less LW radiative warming in the east (Table 4). Rms differences in 1° daily mean LW CRF for the two regions range from 2.5 to 4 W m$^{-2}$ (10%).

Because SW and LW CRF differences in the west Pacific Ocean region have approximately the same magnitude but opposite sign, the difference in net CRF between CERES ERBE-like and SSF results is only 0.1 W m$^{-2}$ (1.4%) (Table 3), whereas the ERBE-like ADMs predict a net cooling in the east that is 1.7 W m$^{-2}$ (8%) larger than SSF.

The above results demonstrate how differences between the ERBE-like and SSF ADMs alone affect CRF. In practice, however, differences in scene identification and temporal sampling can also be important. Scene identification for ERBE is determined from the maximum likelihood estimation (MLE) technique (Wielicki and Green 1989), which uses SW and LW radiances to classify a scene as one of clear, partly cloudy, mostly cloudy, or overcast. ERBE temporal sampling uses directional models defined for the same scene types. The

TABLE 4. Same as Table 3, but for the east Pacific Ocean region (5°S–5°N, 80°–105°W).

| | SW flux (W m$^{-2}$) | | LW flux (W m$^{-2}$) | | SW CRF (W m$^{-2}$) | | LW CRF (W m$^{-2}$) | | Net CRF (W m$^{-2}$) | | $f$ | $\tau$ | $Z_e$ | Count |
|---|---|---|---|---|---|---|---|---|---|---|---|---|---|---|
| | SSF | ES8 | SSF | ES8 | SSF | ES8 | SSF | ES8 | SSF | ES8 | (%) | (−) | (km) | (−) |
| Clear | 40.1 | 36.3 | 282.2 | 283.9 | — | — | — | — | — | — | — | — | — | — |
| Liquid | 75.8 | 72.5 | 268.8 | 271.8 | −35.7 | −36.2 | 13.4 | 12.1 | −22.3 | −24.1 | 45 | 2.02 | 2.67 | 2798 |
| Ice | 124.5 | 120.2 | 219.8 | 223.8 | −84.4 | −83.9 | 62.4 | 60.1 | −22.1 | −23.8 | 73 | 3 | 7.87 | 914 |
| All | 84.7 | 81.3 | 258.4 | 261.5 | −44.7 | −45 | 23.8 | 22.3 | −20.9 | −22.6 | 49 | 2.23 | 3.95 | 3954 |

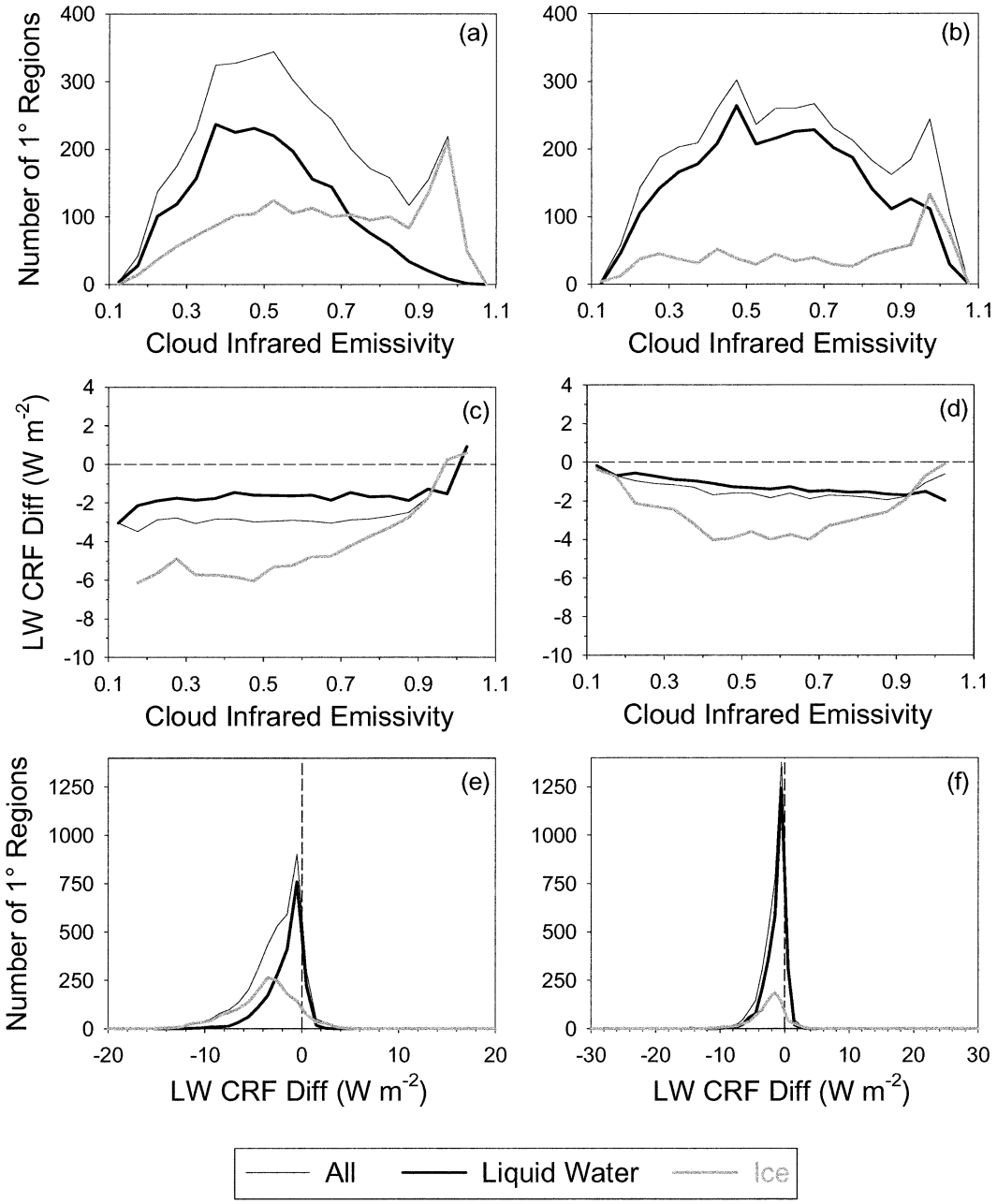


FIG. 14. (a), (b) Distribution of 1° daily mean cloud infrared emissivity, (c), (d) average LW CRF difference against cloud infrared emissivity, and (e), (f) distribution of 1° LW CRF difference (ERBE-like minus SSF) for the (left) west and (right) east Pacific Ocean regions.

CRF sensitivity to all three factors is determined by reprocessing the data for the model combinations provided in Table 5. Results (Fig. 16) show that while CRF is quite sensitive to changes in both ADMs and clear-sky scene identification, it has a weak dependence on the directional models. In the SW, clear scenes identified by the ERBE MLE are brighter by 1–2 W $m^{-2}$ because of undetected boundary layer cloud contamination. In the LW, clear scenes from the ERBE MLE produce TOA fluxes that are 1.4 W $m^{-2}$ larger in the east Pacific Ocean region and 0.3 W $m^{-2}$ smaller in the west. Net CRF sensitivity to clear-sky scene identification is between 1.8 and 3.0 W $m^{-2}$. These differences are smaller than those in a recent paper by Stubenrauch et al. (2002), who compared TOA fluxes for clear scenes identified from ERBE and the International Satellite Cloud Climatology Project (ISCCP). In that study, SW TOA fluxes for ERBE clear scenes

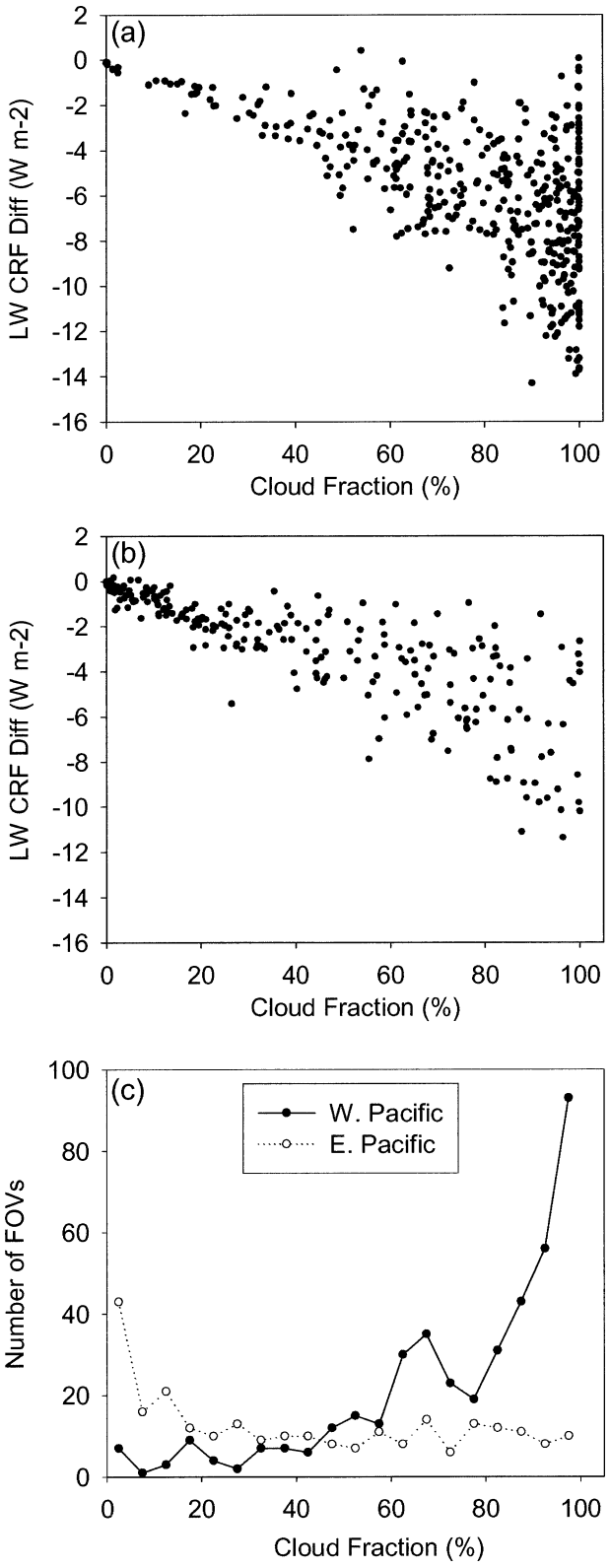


FIG. 15. Scatterplot of 1° daily mean LW CRF difference (ERBE-like minus SSF) against cloud fraction for ice clouds with cloud infrared emissivity less than 0.5 in (a) the west Pacific Ocean region and (b) the east Pacific Ocean region, together with (c) the corresponding cloud fraction frequency of occurrence.

TABLE 5. Comparisons used to determine the TOA flux and cloud radiative forcing sensitivity to differences between SSF (S) and ERBE (E) ADMs, scene identification, and directional models. The (X, Y, Z) arrays correspond to ADMs (X), scene identification (Y), and directional models (Z) used.

| Model | Sensitivity test |
|---|---|
| ADM | (E, S, S)–(S, S, S) |
| Clear-sky scene identification | (E, E, S)–(E, S, S) |
| Directional model | (E, E, E)–(E, E, S) |
| All | (E, E, E)–(S, S, S) |

are actually smaller than ISCCP by 5–10 W $m^{-2}$ and clear-sky LW TOA fluxes are larger by 4 W $m^{-2}$. The sources of the discrepancies are unknown.

The official CERES products that provide monthly average regional TOA fluxes and CRF results are the CERES monthly TOA/surface averages (SRBAVG) and ERBE-like monthly geographic averages (ES4) products. The CERES SRBAVG product consists of monthly 1° regional mean TOA fluxes derived from CERES SSF instantaneous TOA fluxes. The non-GEO data product uses directional models based on the SSF ADMs, while the GEO data product merges CERES measurements with geostationary satellite measurements to more accurately resolve the diurnal variation in TOA fluxes (Young et al. 1998). The CERES ES4 product consists of monthly 2.5° regional mean TOA fluxes derived from ERBE-like instantaneous TOA fluxes and the ERBE directional models (Wong et al. 2000).

Tables 6 and 7 show TOA flux and CRF results for the west and east Pacific Ocean regions during March 1998 and March 2000, respectively. The dramatic difference in TOA fluxes and CRF between these 2 months is due to the strong ENSO event that occurred in early 1998. While ES4, non-GEO and GEO results are generally consistent to within 3 W $m^{-2}$, differences are larger in the eastern Pacific Ocean region in March 1998. For that month, ES4 SW radiative cooling is larger by approximately 6.5 W $m^{-2}$ and LW radiative warming is larger by 5 W $m^{-2}$. One explanation for the larger difference may be related to the dramatic increase in convection in the eastern Pacific Ocean region in March 1998 as compared with normal years. Based on ADM differences alone, an increase in cloud optical depth produces larger ERBE-like SW TOA fluxes (cf. Fig. 11). In the LW, most of the discrepancy (3.4 W $m^{-2}$) is explained by clear-sky LW TOA flux differences. Another factor that may affect the results is the difference in sampling between the ES4 and SRBABVG products. Because the ES4 product does not rely on information from VIRS, it is based on instantaneous TOA fluxes over the entire CERES swath and, thus, uses approximately 2 times the number of measurements as the SBAVG product. If the clouds sampled in the ES4 product for that month happened to be dramatically different from those sampled by the

TABLE 6. TOA flux and CRF (W m$^{-2}$) for Mar 1998 in the west and east Pacific Ocean regions as determined from the CERES SRBAVG and ERBE-like (ES4) products.

| | SW flux (W m$^{-2}$) | | | LW flux (W m$^{-2}$) | | | SW CRF (W m$^{-2}$) | | | LW CRF (W m$^{-2}$) | | | Net CRF (W m$^{-2}$) | | |
|---|---|---|---|---|---|---|---|---|---|---|---|---|---|---|---|
| | ES4 | Non-GEO | GEO | ES4 | Non-GEO | GEO | ES4 | Non-GEO | GEO | ES4 | Non-GEO | GEO | ES4 | Non-GEO | GEO |
| West Pacific Ocean region | | | | | | | | | | | | | | | |
| Clear | 40.6 | 40.7 | 40.7 | 290.8 | 290.3 | 289.3 | — | — | — | — | — | — | — | — | — |
| All | 82.5 | 83.1 | 81.9 | 262.7 | 261.2 | 261.7 | −41.9 | −42.4 | −41.2 | 28.0 | 29.0 | 27.6 | −13.9 | −13.4 | −13.6 |
| East Pacific Ocean region | | | | | | | | | | | | | | | |
| Clear | 39.4 | 41.2 | 41.2 | 283.16 | 281.5 | 279.8 | — | — | — | — | — | — | — | — | — |
| All | 120.1 | 115.1 | 115.4 | 221.20 | 223.5 | 222.9 | −80.7 | −73.8 | −74.2 | 62.0 | 58.0 | 56.9 | −18.7 | −15.8 | −17.3 |

SRBAVG product, this cloud also cause larger differences.

## 4. Discussion

Results in the preceding sections clearly demonstrate the improvement in TOA flux accuracy from the CERES SSF product over the CERES ERBE-like product. Part of this improvement is because the CERES TRMM ADMs were developed and applied using measurements with the same spatial resolution and scene identification. In contrast, the ERBE ADMs were developed using 90-km-resolution *Nimbus-7* Earth Radiation Budget (ERB) scanner data with scene identification from the Temperature and Humidity Infrared Radiometer (THIR) and the Total Ozone Mapping Spectrometer (TOMS) and are applied to 10-km CERES TRMM measurements using the MLE scene-identification technique (Wielicki and Green 1989). Consequently, inconsistencies in the manner in which the ERBE ADMs were developed and applied may introduce errors in the CERES ERBE-like product that are not present in the CERES SSF results. Another important reason for the improvement is the increase in the number of CERES TRMM ADM scene types and the far superior scene identification from VIRS.

Despite these improvements, it must be noted that because the VIRS scene identification relies on several assumptions for detecting clouds and inferring their optical properties, larger-than-average instantaneous TOA flux errors are expected in certain conditions. These include multilayer cloud conditions, where conventional passive remote sensing threshold techniques often fail to even identify more than one cloud layer (Baum and Spinhirne 2000), in the presence of vertically extensive clouds, where 3D effects such as cloud shadows and enhanced cloud-side illumination can result in anisotropic patterns that deviate significantly from average conditions, and in regions where topographical variations are pronounced. Such conditions likely play a key role in explaining systematic angle-dependent biases in observed large-ensemble averages of cloud fraction (Minnis 1989), cloud optical depth retrievals (Loeb and Davies 1996; Loeb and Coakley 1998), and LW surface anisotropy (Minnis and Khaiyer 2000). Another situation in which instantaneous TOA flux errors are likely to be larger is in sunglint over water surfaces, which can occur in clear, broken, and thin overcast cloud conditions. In sunglint the anisotropy changes very rapidly with observation angle and the relatively coarse angular bins used to define the CERES ADMs cannot resolve such variability.

A more subtle effect that has yet to be quantified is the influence of CERES FOV growth with viewing zenith angle on ADM-derived TOA fluxes. The equivalent circle diameter of a CERES TRMM footprint increases from 10 km at nadir to 45 km at $\theta = 70°$, and reaches 95 km at $\theta = 80°$. Because ADMs are

TABLE 7. Same as Table 6, but for Mar 2000.

| | SW flux (W m$^{-2}$) | | | LW flux (W m$^{-2}$) | | | SW CRF (W m$^{-2}$) | | | LW CRF (W m$^{-2}$) | | | Net CRF (W m$^{-2}$) | | |
|---|---|---|---|---|---|---|---|---|---|---|---|---|---|---|---|
| | ES4 | Non-GEO | GEO | ES4 | Non-GEO | GEO | ES4 | Non-GEO | GEO | ES4 | Non-GEO | GEO | ES4 | Non-GEO | GEO |
| West Pacific Ocean region | | | | | | | | | | | | | | | |
| Clear | 40.4 | 41.2 | 41.2 | 287.2 | 288.0 | 286.2 | — | — | — | — | — | — | — | — | — |
| All | 91.4 | 89.4 | 92.4 | 240.5 | 243.1 | 242.3 | −51.0 | −48.2 | −51.2 | 46.7 | 44.9 | 43.8 | −4.2 | −3.3 | −7.4 |
| East Pacific Ocean region | | | | | | | | | | | | | | | |
| Clear | 39.6 | 41.1 | 41.1 | 283.9 | 282.0 | 280.7 | — | — | — | — | — | — | — | — | — |
| All | 84.0 | 86.4 | 87.0 | 259.7 | 257.6 | 257.1 | −44.4 | −45.3 | −45.9 | 24.2 | 24.4 | 23.6 | −20.2 | −20.9 | −22.3 |

constructed by compositing CERES radiances for the same ''scene type'' into angular bins, the anisotropy of a given scene type is, thus, determined from FOVs whose spatial resolution varies by at least an order of magnitude. Ye and Coakley (1996) demonstrated that FOV growth with viewing zenith angle has a significant effect on the ERBE scene identification. More study is needed to quantify how this affects TOA fluxes from ADMs based on imager scene identification.

Also note that because cloud properties depend on cloud size, and because the CERES FOV size increases with viewing zenith angle, cloud populations defined by a given set of criteria at nadir may have very different characteristics from those defined by the same criteria at oblique CERES viewing zenith angles. As an example, Figs. 17a and 17b show TOA albedo and LW TOA flux against CERES viewing zenith angle for overcast scenes from nine alongtrack days. Albedo increases with viewing zenith angle from 0.416 to 0.458, and LW flux decreases from 211.8 to 195.3 W m$^{-2}$. These large changes in albedo and LW flux with CERES viewing zenith angle are not due to ADM errors, but rather to changes in the physical properties of overcast clouds with CERES FOV size. This is clearly evident from the FOV-averaged imager cloud optical depth and cloud-top temperature retrievals in Figs. 17a and 17b. When CERES is in the alongtrack scan mode, the imager observes all CERES FOVs from near-nadir VIRS viewing zenith angles within approximately 2 min. Therefore, from the imager vantage point, an increase in CERES viewing zenith angle corresponds only to an increase in the size of the overcast scene. As the horizontal extent of the overcast clouds increases with CERES viewing zenith angle, results in Figs. 17a and 17b show that cloud optical depth increases and cloud-top temperature decreases. These changes are associated with an increase in TOA albedo and a decrease in LW TOA flux. One method of reducing this dependence on FOV size is to use more parameters to define the scene type. For example, by defining the cloud population by discrete intervals of cloud fraction, optical depth, phase, and so on, the cloud population will have similar physical properties over a wide range of spatial scales. Note that while the physical properties of the clouds will be less sensitive to FOV size, their frequency of occurrence will still depend strongly on FOV size. An alternate method of reducing the dependence on FOV size is to average CERES FOVs together to create a more constant FOV size at different viewing zenith angles. Ye and Coakley (1996) use this approach to analyze ERBE data.

## 5. Summary

The CERES TRMM single scanner footprint (SSF) product provides broadband TOA radiative fluxes over the Tropics in the SW, LW, and WN regions, coincident imager-derived cloud and aerosol properties, and at-

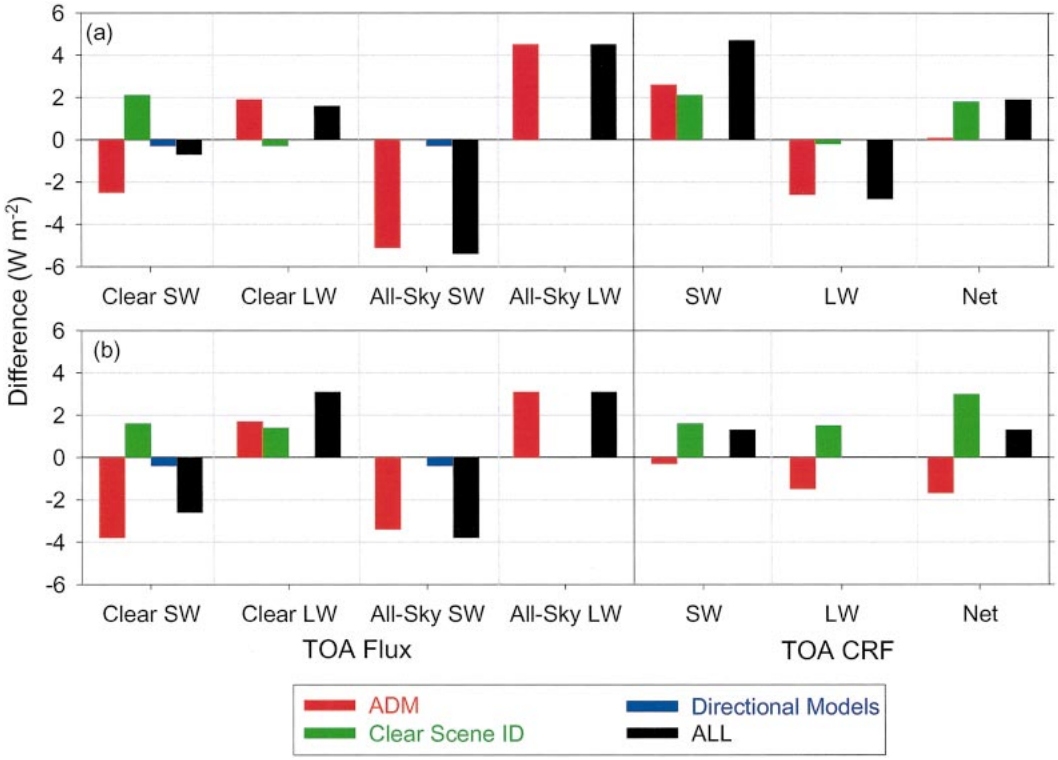


FIG. 16. SW and LW TOA flux and CRF sensitivity to SSF and ERBE-like ADMs, clear-sky scene identification, and directional model differences in (a) the west Pacific Ocean region and (b) the east Pacific Ocean region.

mospheric state parameters from 4D assimilation products. One of the major advances in CERES is the availability of improved ADMs for estimating TOA radiative fluxes from broadband radiance measurements. Multiangle CERES measurements and coincident imager cloud information are used to construct empirical ADMs for scene types defined by parameters that have a strong influence on the anisotropy (or angular dependence) of TOA radiances. (The CERES TRMM ADMs are available for viewing and downloading at the following Web address: http://asd-www.larc.nasa.gov/Inversion/.)

The advantages of combining CERES and imager data are demonstrated by comparing TOA fluxes from the CERES SSF and ERBE-like products. The CERES SSF product uses the new CERES ADMs and imager scene identification, whereas fluxes in the ERBE-like product are based on ADMs and scene identification developed during the ERBE experiment for only 12 scene types. When stratified by sun–Earth–satellite

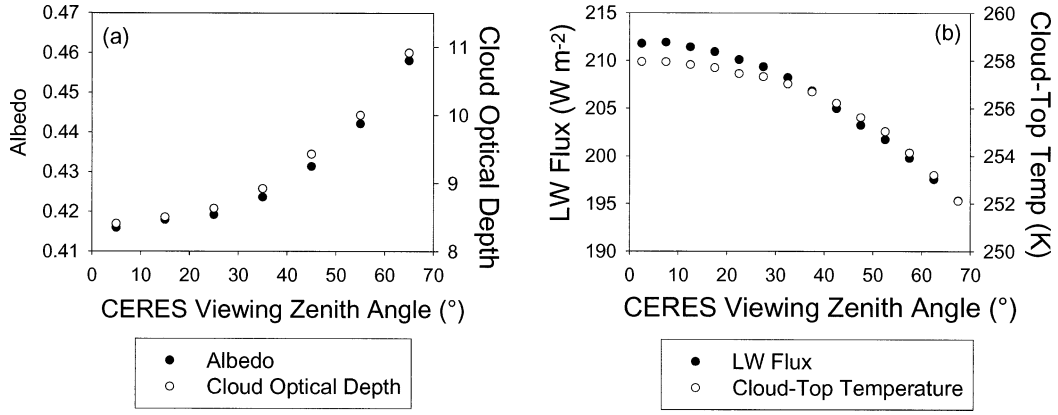


FIG. 17. (a) TOA albedo ($\theta_0$ = 40°–50°) and cloud optical depth, and (b) LW TOA flux and cloud-top temperature against CERES viewing zenith angle for overcast scenes from nine alongtrack days.

viewing geometry, all-sky mean TOA fluxes from the new CERES ADMs are consistent to within 2% in the SW and 0.7% (or 2 W $m^{-2}$) in the LW. In contrast, ERBE-like mean fluxes show a systematic dependence on viewing zenith angle of 10% in the SW and 3.5% (or 9 W $m^{-2}$) in the LW. Regional TOA flux uncertainties from the CERES SSF is found to be $<0.5$ W $m^{-2}$ both in the SW and LW, which is within prelaunch CERES accuracy goals set by Wielicki et al. (1995). Multiangle consistency checks show that 1° regional instantaneous TOA flux errors from the new CERES ADMs are smaller than those from the ERBE ADMs by factors of 2.2 and 1.68 in the SW and LW, respectively, for all-sky conditions. We estimate that 1° regional instantaneous TOA fluxes are accurate to within 10 W $m^{-2}$ in the SW and 3.5 W $m^{-2}$ in the LW, with little dependence on cloud phase, cloud optical depth (SW), or infrared cloud emissivity (LW). In contrast, TOA flux errors from the ERBE-like product are a strong function of these parameters—ERBE-like TOA flux errors are larger than SSF errors by factors of 3–4 for thin ice clouds, and 3–6 for thick liquid water and ice clouds.

Cloud radiative forcing (CRF) sensitivity to ADM differences is estimated from instantaneous ERBE-like and SSF TOA fluxes converted to 1° regional daily mean clear (according to VIRS) and all-sky TOA fluxes for two regions in the west and east Pacific Ocean. While rms differences in CRF are typically 7–8 W $m^{-2}$ in the SW and 2.5–4.0 W $m^{-2}$ in the LW, differences in average CRF are typically between 0–3 W $m^{-2}$ in the SW and 1.5–2.5 W $m^{-2}$ in the LW. These differences are comparable in magnitude to those resulting from a change in clear-sky scene identification from the ERBE MLE to the VIRS imager.

New global ADMs are currently being developed for the CERES instruments on the *Terra* (launched on 18 December 1999) and *Aqua* (launched on 4 May 2002) spacecrafts. Scene identification will take advantage of the new capabilities of the Moderate Resolution Imaging Spectroradiometer (MODIS). These new ADMs will be based on at least 2 yr of global measurements from each instrument, which will provide sufficient sampling to increase the ADM angular resolution and number of scene types. As with CERES TRMM, an extensive set of validation activities will be performed to evaluate the new ADMs and their resulting TOA fluxes.

*Acknowledgments*. This research was funded by the Clouds and the Earth's Radiant Energy System (CERES) project under NASA Grant NAG-1-2318. Funding was also provided from NASA Grant NAG-1-01096. The authors thank Drs. Takmeng Wong, Donald P. Garber, and Mr. Edward A. Kizer for their help in ERBE-like and SRBAVG data analysis.

## REFERENCES

Barkstrom, B. R., 1984: The Earth Radiation Budget Experiment (ERBE). *Bull. Amer. Meteor. Soc.*, **65,** 1170–1186.

Baum, B. A., and J. D. Spinhirne, 2000: Remote sensing of cloud properties using MODIS Airborne Simulator imagery during SUCCESS. III. Cloud overlap. *J. Geophys. Res.,* **105,** 11 793–11 804.

Berk, A., G. P. Anderson, P. K. Acharya, J. H. Chetwynd, L. S. Bernstein, E. P. Shettle, M. W. Matthew, and S. M. Adler-Golden, 1999: MODTRAN4 User's Manual. Air Force Research Laboratory/Space Vehicles Directorate, Hanscom Air Force Base, 94 pp.

Brooks, D. R., E. F. Harrison, P. Minnis, J. T. Suttles, and R. S. Kandel, 1986: Development of algorithms for understanding the temporal and spatial variability of the earth's radiation balance. *Rev. Geophys.,* **24,** 422–438.

Cess, R. D., M. Zhang, B. A. Wielicki, D. F. Young, X.-L. Zhou, and Y. Nikitenko, 2001: The influence of the 1998 El Niño upon cloud-radiative forcing over the Pacific warm pool. *J. Climate,* **14,** 2129–2137.

Chambers, L., L. Bing, B. A. Wielicki, Y. Hu, and K.-M. Xu, 2002: Reply. *J. Climate,* **15,** 2716–2717.

Geier, E. B., R. N. Green, D. P. Kratz, P. Minnis, W. F. Miller, S. K. Nolan, and C. B. Franklin, 2003: Single satellite footprint TOA/surface fluxes and clouds (SSF) collection document. Release 2, version 1, NASA Langley Research Center, 243 pp. [Available online at http://asd-www.larc.nasa.gov/ceres/collect_guide/.]

Harrison, E. F., P. Minnis, B. R. Barkstrom, V. Ramanathan, R. D. Cess, and G. G. Gibson, 1990: Seasonal variation of cloud radiative forcing derived from the Earth Radiation Budget Experiment. *J. Geophys. Res.,* **95,** 18 687–18 703.

Kummerow, C., W. Barnes, T. Kozu, J. Shiue, and J. Simpson, 1998: The Tropical Rainfall Measuring Mission (TRMM) sensor package. *J. Atmos. Oceanic Technol.,* **15,** 809–817.

Lin, B., B. A. Wielicki, L. H. Chambers, Y. Hu, and K.-M. Xu, 2002: The iris hypothesis: A negative or positive cloud feedback? *J. Climate,* **15,** 3–7.

Lindzen, R., M.-D. Chou, and A. Hou, 2001: Does the earth have an adaptive infrared iris? *Bull. Amer. Meteor. Soc.,* **82,** 417–432.

Loeb, N. G., and R. Davies, 1996: Observational evidence of plane parallel model biases: The apparent dependence of cloud optical depth on solar zenith angle. *J. Geophys. Res.,* **101,** 1621–1634.

——, and J. A. Coakley Jr., 1998: Inference of marine stratus cloud optical depths from satellite measurements: Does 1D theory apply? *J. Climate,* **11,** 215–233.

——, F. Parol, J.-C. Buriez, and C. Vanbauce, 2000: Top-of-atmosphere albedo estimation from angular distribution models using scene identification from satellite cloud property retrievals. *J. Climate,* **13,** 1269–1285.

——, K. J. Priestley, D. P. Kratz, E. B. Geier, R. N. Green, B. A. Wielieki, P. O'R. Hinton, and S. K. Nolan, 2001: Determination of unfiltered radiances from the Clouds and the Earth's Radiant Energy System (CERES) instrument. *J. Appl. Meteor.,* **40,** 822–835.

——, S. Kato, N. M. Smith, S. K. Gupta, W. F. Miller, P. Minnis, and B. A. Wielicki, 2003: Angular distribution models for top-of-atmosphere radiative flux estimation from the Clouds and the Earth's Radiant Energy System instrument on the Tropical Rainfall Measuring Mission Satellite. Part I: Methodology. *J. Appl. Meteor.,* **42,** 240–265.

Minnis, P., 1989: Viewing zenith angle dependence of cloudiness determined from coincident GOES East and GOES West data. *J. Geophys. Res.,* **94,** 2303–2320.

——, and M. M. Khaiyer, 2000: Anisotropy of land surface skin temperature derived from satellite data. *J. Appl. Meteor.,* **39,** 1117–1129.

Nakajima, T., and M. Tanaka, 1986: Matrix formulations for the transfer of solar radiation in a plane-parallel scattering atmosphere. *J. Quant. Spectros. Radiat. Transfer,* **35,** 13–21.

Payette, F., 1989: Applications of a sampling strategy for the ERBE scanner data. M.S. thesis, Dept. of Atmospheric and Oceanic Sciences, McGill University, 100 pp.

Priestley, K. J., R. B. Lee III, R. N. Green, S. Thomas, and R. S. Wilson, 1999: Radiometric performance of the Clouds and the Earth's Radiant Energy System (CERES) proto-flight model on the Tropical Rainfall Measuring Mission (TRMM) spacecraft for 1998. Preprints, *10th Conf. on Atmospheric Radiation,* Madison, WI, Amer. Meteor. Soc., 33–36.

Rabier, F., J.-N. Thepaut, and P. Courtier, 1998: Extended assimilation and forecast experiments with a four-dimensional variational assimilation. *Quart. J. Roy. Meteor. Soc.,* **124,** 1861–1887.

Ramanathan, V., R. D. Cess, E. F. Harrison, P. Minnis, B. R. Barkstrom, E. Ahmad, and D. Hartmann, 1989: Cloud-radiative forcing and climate: Results from the Earth Radiation Budget Experiment. *Science,* **243,** 57–63.

Smith, G. L., 1994: Effects of time response on the point spread function of a scanning radiometer. *Appl. Opt.,* **33,** 7031–7037.

——, R. N. Green, E. Raschke, L. M. Avis, J. T. Suttles, B. A. Wielicki, and R. Davies, 1986: Inversion methods for satellite studies of the earth radiation budget: Development of algorithms for the ERBE mission. *Rev. Geophys.,* **24,** 407–421.

Stubenrauch, C. J., V. Briand, and W. B. Rossow, 2002: The role of clear-sky identification in the study of cloud radiative effects: Combined analysis from ISCCP and the Scanner of Radiation Budget. *J. Appl. Meteor.,* **41,** 396–412.

Suttles, J. T., and Coauthors, 1988: Angular radiation models for Earth-atmosphere systems, Vol. I—Shortwave radiation. NASA Rep. RP-1184, 144 pp.

——, ——, G. L. Smith, B. A. Wielicki, I. J. Walker, V. R. Taylor, and L. L. Stowe, 1989: Angular radiation models for Earth-atmosphere systems, Vol. II—Longwave radiation. NASA Rep. RP-1184, 84 pp.

——, B. A. Wielicki, and S. Vemury, 1992: Top-of-atmosphere radiative fluxes: Validation of ERBE scanner inversion algorithm using *Nimbus-7* ERB data. *J. Appl. Meteor.,* **31,** 784–796.

Wielicki, B. A., and R. N. Green, 1989: Cloud identification for ERBE radiation flux retrieval. *J. Appl. Meteor.,* **28,** 1133–1146.

——, R. D. Cess, M. D. King, D. A. Randall, and E. F. Harrison, 1995: Mission to planet Earth: Role of clouds and radiation in climate. *Bull. Amer. Meteor. Soc.,* **76,** 2125–2152.

Wong, T., D. F. Young, M. Haeffelin, and S. Weckmann, 2000: Validation of the CERES/TRMM ERBE-like monthly mean clear-sky longwave dataset and the effects of the 1998 ENSO event. *J. Climate,* **13,** 4256–4267.

Ye, Q., and J. A. Coakley Jr., 1996: Biases in Earth radiation budget observations, Part 2: Consistent scene identification and anisotropic factors. *J. Geophys. Res.,* **101,** 21 253–21 263.

Young, D. F., P. Minnis, D. R. Doelling, G. G. Gibson, and T. Wong, 1998: Temporal interpolation methods for the Clouds and the Earth's Radiant Energy System (CERES) experiment. *J. Appl. Meteor.,* **37,** 572–590.